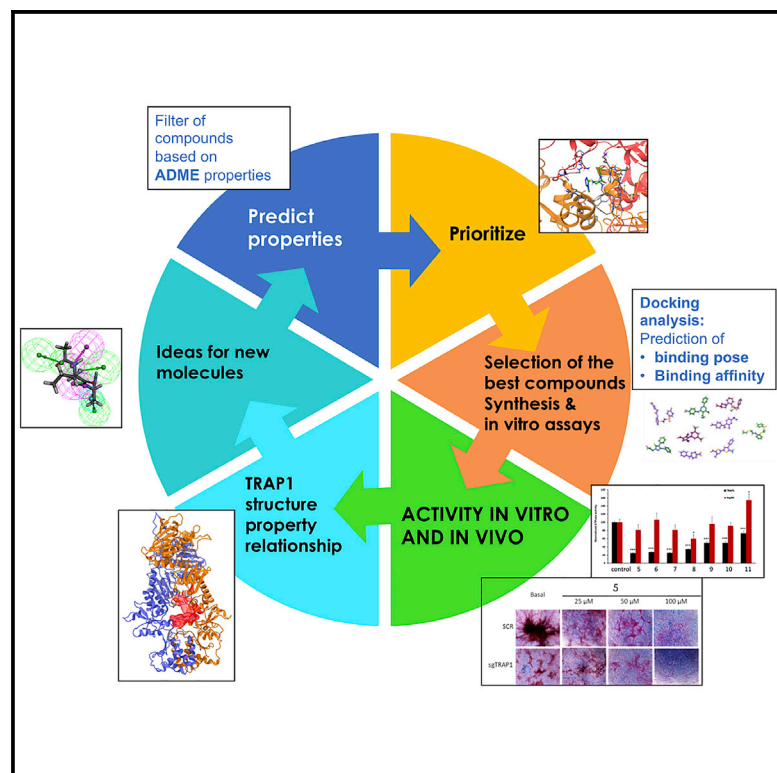


Rational Design of Allosteric and Selective Inhibitors of the Molecular Chaperone TRAP1

Graphical Abstract



Authors

Carlos Sanchez-Martin,
Elisabetta Moroni,
Mariasosaria Ferraro, ..., Paolo Quadrelli,
Andrea Rasola, Giorgio Colombo

Correspondence

andrea.rasola@unipd.it (A.R.),
g.colombo@unipv.it (G.C.)

In Brief

The molecular chaperone TRAP1 regulates energy metabolism, and its activity is relevant in cancer and degenerative diseases. Here, Sanchez-Martin et al. identify highly selective allosteric inhibitors of TRAP1. These compounds revert biochemical and pro-neoplastic effects of TRAP1 and could both enlighten its mode of action and disclose novel therapeutic strategies.

Highlights

- Analysis of TRAP1 dynamics allows discovery of paralog-selective allosteric inhibitors
- Small molecules targeting TRAP1 revert TRAP1-dependent succinate dehydrogenase inhibition
- Allosteric TRAP1 inhibitors abolish tumorigenic growth of neoplastic cells
- Selective targeting of TRAP1 activity provides new antagonists of chaperones



Rational Design of Allosteric and Selective Inhibitors of the Molecular Chaperone TRAP1

Carlos Sanchez-Martin,^{1,4} Elisabetta Moroni,^{2,4} Mariarosaria Ferraro,^{2,4} Claudio Laquatra,¹ Giuseppe Cannino,¹ Ionica Masgras,¹ Alessandro Negro,¹ Paolo Quadrelli,³ Andrea Rasola,^{1,*} and Giorgio Colombo^{2,3,5,*}

¹Dipartimento di Scienze Biomediche, Università di Padova, viale G. Colombo 3, 35131 Padova, Italy

²Istituto di Scienze e Tecnologie Chimiche “Giulio Natta”–SCITEC, Via Mario Bianco 9, 20131 Milano, Italy

³Dipartimento di Chimica, Università di Pavia, via Taramelli 12, 27100 Pavia, Italy

⁴These authors contributed equally

⁵Lead Contact

*Correspondence: andrea.rasola@unipd.it (A.R.), g.colombo@unipv.it (G.C.)

<https://doi.org/10.1016/j.celrep.2020.107531>

SUMMARY

TRAP1 is the mitochondrial paralog of the heat shock protein 90 (HSP90) chaperone family. Its activity as an energy metabolism regulator has important implications in cancer, neurodegeneration, and ischemia. Selective inhibitors of TRAP1 could inform on its mechanisms of action and set the stage for targeted drug development, but their identification was hampered by the similarity among active sites in HSP90 homologs. We use a dynamics-based approach to identify a TRAP1 allosteric pocket distal to its active site that can host drug-like molecules, and we select small molecules with optimal stereochemical features to target the pocket. These leads inhibit TRAP1, but not HSP90, ATPase activity and revert TRAP1-dependent downregulation of succinate dehydrogenase activity in cancer cells and in zebrafish larvae. TRAP1 inhibitors are not toxic per se, but they abolish tumorigenic growth of neoplastic cells. Our results indicate that exploiting conformational dynamics can expand the chemical space of chaperone antagonists to TRAP1-specific inhibitors with wide therapeutic opportunities.

INTRODUCTION

Members of the heat shock protein 90 (HSP90) family of proteins oversee a broad range of functions that include quality control in client protein folding, trafficking, and activity regulation of signaling molecules, assembly and disassembly of multiprotein complexes, and stabilization of resistance traits in protein drug targets (Karagöz and Rüdiger, 2015; Taipale et al., 2010). These biochemical tasks require sequential cycles of ATPase activity, whereby binding, hydrolysis, and release of the nucleotide drive the conformational changes of the client that tune downstream biological effects (Schopf et al., 2017). Targeting the ATP pocket by small molecules has proven a viable strategy for the inactivation of HSP90 family chaperone functions, and ATP-competitive

inhibitors have demonstrated potent activities in models of cancer, neurodegeneration, infections, and inflammatory diseases (Shrestha et al., 2016). However, catalytic sites of the different HSP90 family proteins are highly similar, and most of the current ATP-competitive inhibitors indiscriminately influence the whole functional spectrum of these chaperones. This lack of selectivity results in overall client destabilization that can lead to toxicity, preventing further progress into clinical use. Hence chemical tools that target HSP90 chaperones in paralog-specific ways are currently lacking and highly needed.

TRAP1 is the mitochondrial member of the HSP90 family and an important bioenergetic regulator, because it inhibits both cytochrome *c* oxidase, an oxidative phosphorylation (OXPHOS) component, and succinate dehydrogenase (SDH) at the intersection between OXPHOS and tricarboxylic acid cycle (Sciakovelli et al., 2013; Yoshida et al., 2013). TRAP1 also provides resistance to oxidative stress (Guzzo et al., 2014) and counteracts mitochondrial permeability transition and the ensuing cell death (Bernardi et al., 2015). In tumors, these TRAP1 activities contribute to the metabolic switch of cells toward aerobic glycolysis (i.e., decreased OXPHOS activity paralleled by enhanced glycolysis) and to the resistance to oxidative insults (Masgras et al., 2017b), and TRAP1-dependent inhibition of SDH prompts stabilization of HIF1 α (Sciakovelli et al., 2013), a transcription factor with crucial pro-neoplastic activities (Semenza, 2013). TRAP1 expression is induced in many cancer types (Kowalik et al., 2016; Rasola et al., 2014), where it correlates with progression, metastasis, and disease recurrence, and its genetic ablation hampers growth of several neoplastic models (Masgras et al., 2017a, 2017b). However, TRAP1 effects on mitochondrial bioenergetics are not fully elucidated, and the biological outcomes of its activity as a metabolic regulator could be complex and highly context dependent. Accordingly, TRAP1 expression levels are reported to inversely correlate with tumor grade in specific neoplastic settings (Amoroso et al., 2016; Yoshida et al., 2013), in sharp contrast with its proposed pro-neoplastic role. TRAP1 is also important in non-tumor pathological states. Indeed, it acts as an energy rheostat and mitochondrial quality gatekeeper in neurons, and these functions are severely impaired in parkinsonism (Butler et al., 2012; Costa et al., 2013; Fitzgerald et al., 2017; Zhang et al., 2013), whereas in



astrocytes and cardiomyocytes, TRAP1 protects from ischemic damage (Voloboueva et al., 2008; Xiang et al., 2010).

Therefore, compounds that selectively target TRAP1 would constitute useful tools both to disentangle the intricacies of its functions on metabolic and survival networks in the proper intracellular environment, and to translate the modulation of these circuitries into clinical applications.

A peculiar property of TRAP1 chaperone cycle is that ATP binding prompts buckling of one of the two protomers. A first ATP hydrolysis flips asymmetry to the second monomer, inducing its ATPase activity and completion of the cycle (Elnatan et al., 2017; Moroni et al., 2018). Here, we set out to exploit this asymmetry to design selective allosteric chemical tools that, upon TRAP1 binding, could propagate structural changes to distal regions, perturbing mechanisms that govern TRAP1 ATPase or client binding/release cycles and eventually modulating its chaperone activity. Our molecular design strategy is based on data from the recent investigation we conducted on the relationships between nucleotide binding at the N-terminal domain (NTD) and modulation of the structural dynamics of the client-binding region in the large sub-region of the middle domain (LMD). This region acts as a sensor for the conformational signal encoded by the nucleotide (Moroni et al., 2018), so that targeting it with *ad hoc* ligands can expectedly lead to selective perturbation of the whole TRAP1 system. We selected small molecules with optimal stereoelectronic properties to adapt to the dynamic conformations of the client-binding region. We then tested selected ligands in biochemical, cellular, and *in vivo* experiments, demonstrating that they perturb TRAP1 ATPase activity in a selective way; impact the enzymatic function of SDH, a TRAP1 client protein, both in cancer cells and in zebrafish larvae; and abrogate cell tumorigenicity. Therefore, allosteric inhibitors selectively interfere with functional processes regulated by TRAP1 and can be evolved toward perspective therapeutic intervention. Finally, our results open the possibility to expand the molecular diversity space of ligands for the selective targeting of specific members of the HSP90 family of proteins.

RESULTS

Computational Design of TRAP1-Selective Allosteric Ligands

Our design strategy starts from the identification of protein regions involved in long-range allosteric communication with the catalytic site located in the NTD. When targeted by small molecules, distal allosteric regions can aptly transfer the perturbation to the substructure that controls ATP hydrolysis without having to compete with the abundant endogenous substrate, thus perturbing the functional states of the protein.

The presence of ATP in the NTDs generates a conformational signal that is relayed throughout the protein via specific secondary-structure motifs (for details, see Moroni et al., 2018). The identification of distal pockets, dynamically coordinated with the ATP binding site, with stereoelectronic properties compatible with hosting a drug-like molecule (druggable pockets), was thus used to select TRAP1-selective allosteric ligands. We evaluated the dynamic coordination between the ATP site and distal protein residues by means of the coordination propensity (CP)

parameter. CP describes coordination as a function of the mean-square fluctuations of the distance between residues pairs, calculated from molecular dynamics (MD) trajectories (Moroni et al., 2018; Morra et al., 2012). In this model, low CP values between distal pairs predict mechanically coupled regions involved in the long-range propagation of signals. CP analysis was applied to the double ATP-bound dimer of TRAP1 to filter out the regions that are consistently coordinated to the ATP site (the latter defined by 130–141, 173, 176–178, 182, 186, 187, 192–196, 213–221, 234, 266, 268, 417, labeling from the PDB: 4IPE.pdb structure) (Moroni et al., 2018). The identification of druggable pockets in such regions guided the search for TRAP1-selective allosteric ligands.

CP analysis indicated that the conformational signals originated by ATP at either catalytic site in the NTDs were consistently directed toward the same protein region in the LMD of the Straight protomer (also labeled protomer B) (Figures 1A and 1B), reflecting the exquisite structural asymmetry of TRAP1. Specifically, residues of the ATP binding site of the Buckled chain (labeled protomer A) are connected with residues 338–360 and 447–459 in the LMD of the Straight protomer, whereas residues of the ATP binding sites of the Straight protomer are connected with residues 455–466 in the LMD of the same chain (Figure 1A). Interestingly, the observation of the communication between the ATPase site and the middle domain (M-domain) is consistent with recent findings by Schulze et al. (2016), who conducted a study based on the combination between photo-induced electron transfer (PET) spectroscopy and nanosecond single-molecule fluorescence to probe rapid protein dynamics. Using yeast HSP90 as a model, the authors showed that perturbation of the intrasubunit interactions between NTD and M-domain strongly reverberate on measured ATPase activities.

On these bases, we hypothesized that the peculiar asymmetric features of TRAP1, not observed in other isoforms, could define promising TRAP1-specific allosteric hotspots. Accordingly, when we subjected the LMD portion of TRAP1 to structural investigation for detecting potential binding pockets (see STAR Methods), we identified a site that showed a molecular volume suitable to host drug-like compounds. The pocket was consistently present in the most populated structural ensembles and characterized by a large positively charged area formed by the side chains of residues Arg341 and Lys364, flanked by a negatively charged region due to residues Glu457 and Asp458, and at the opposite side, by another negative region formed by residues Glu647 and Glu648. The two negatively charged regions are separated by a large hydrophobic one, formed by residues Pro361, Met363, Pro365, Val370, Leu461, and Phe378 (Figures 1C and 1D).

We used the chemical and conformational properties of the pocket as a template for the development of a six-feature pharmacophore model aimed at recapitulating the complementary interactions necessary for a ligand to productively bind the site (Figure 1D). Next, we screened both the National Cancer Institute (NCI) and ZINC databases with the pharmacophore, and retrieved hits were post-processed and further filtered for their drug-like, ADME (absorption, distribution, metabolism, and excretion) properties and docking scores to the predicted pocket (see STAR Methods).

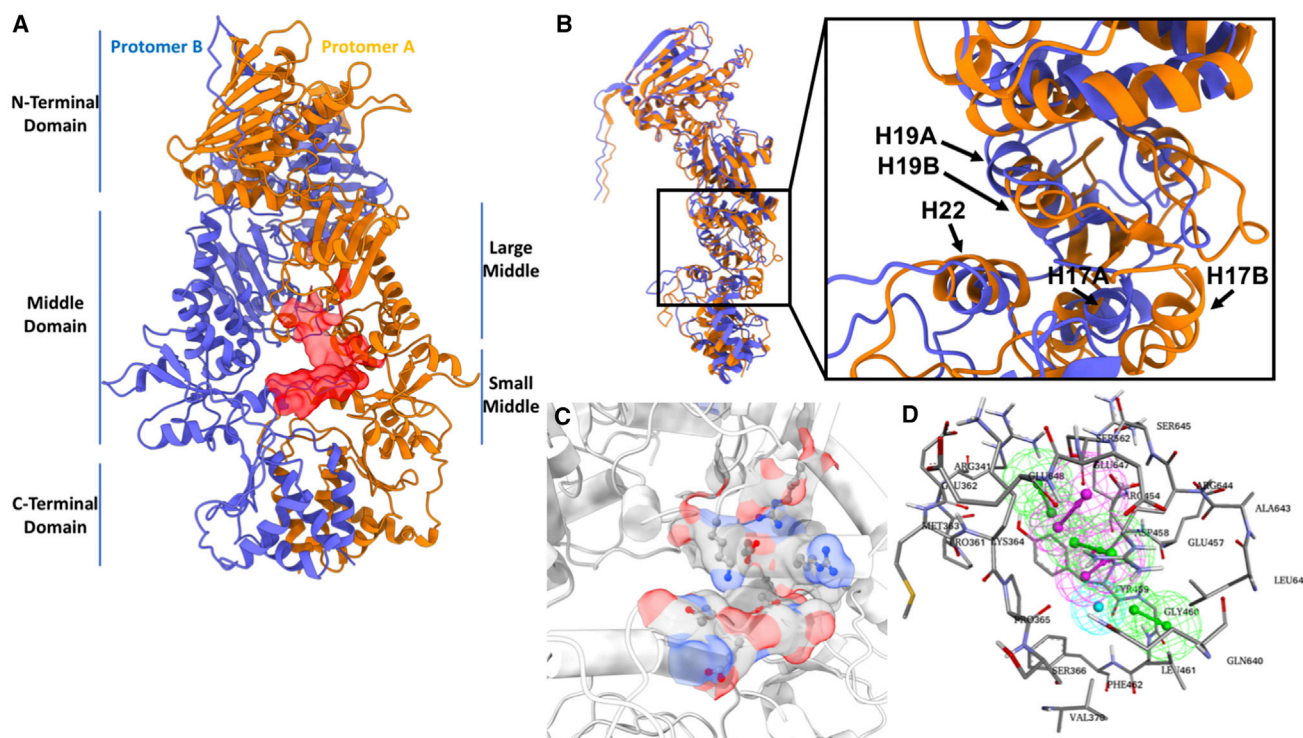


Figure 1. Structure- and Dynamics-Based Selection of TRAP1 Allosteric Ligands

- (A) The structure of the protein with the two protomers represented in different colors; the identified allosteric pocket is indicated in the form of a red-colored surface.
- (B) Superimposition of protomer A (straight protomer) and protomer B (buckled protomer). The asymmetry region is highlighted and zoomed out. Labels correspond to the different helix names.
- (C) A zoom in on the allosteric pocket. In this case, the surface is colored according to the chemical properties of the constituting residues.
- (D) The full pharmacophore used for molecular selection.

At the end of the process, 11 hits could be retrieved and purchased for testing. On the basis of their structures, the retrieved compounds were grouped into two subsets labeled large and small. The former group contains molecules 1–4, with a molecular weight close to 500. These compounds could be further optimized via the addition of different substituents and decorations. The latter set contains lower molecular weight, fragment-like molecules 5–11, which could be prospectively evolved into more active hits through coupling and fusion steps. The structures of the selected molecules are shown and labeled in Figure 2.

A Structure- and Dynamics-Based Model of TRAP1 Allosteric Inhibition

The complexes between allosteric inhibitors and members of the HSP90 family have proved refractory to crystallization (Ferraro et al., 2019). TRAP1 is no exception, and our attempts to obtain crystals of the complexes failed. Therefore, we used molecular simulations to develop a molecular model of the inhibition mechanisms of identified compounds. We selected for this analysis compounds 5, 6, and 7, which turned out to be the most active hits (see Figures 4B and 4C), and generated docking models of their allosteric complexes with TRAP1. In all of the complexes with inhibitors docked at the identified allosteric pocket, the

NTD catalytic sites are occupied by ATP. Each of the three protein–ligand complexes (allosteric inhibitor+ATP) was simulated using three independent replicates, resulting in a total of 2.7 μ s (900 ns \times 3) of MD simulations. The allosteric ligand-bound complexes were compared with analogous simulations of double-ATP TRAP1 (900 ns), to characterize the patterns of inhibitor-induced internal dynamics and long-range and domain-domain (de)coupling.

We first identified the TRAP1 residues able to establish the most stable interactions with our compounds: such residues were identified through their maximum occupancy time, which is the longest time a given residue spends within 4 Å from the ligand in the ensemble of conformations obtained by combining all of the trajectories for each ligand (meta-trajectory) (Table S1). The most contacted residues (maximum occupancy time >20% of the total time) were then used to generate an MD-refined fingerprint of the allosteric pocket and to describe the binding dynamics by clustering ligand conformations.

As expected from the small size of the most active compounds, these hits were found to explore at least three representative binding modes in the site (Figure S1), capturing from 88.1% to 95% of the conformations sampled along their respective meta-trajectories (Table S2). All compounds were found to interact with Tyr459. Together with Phe401, this residue is part

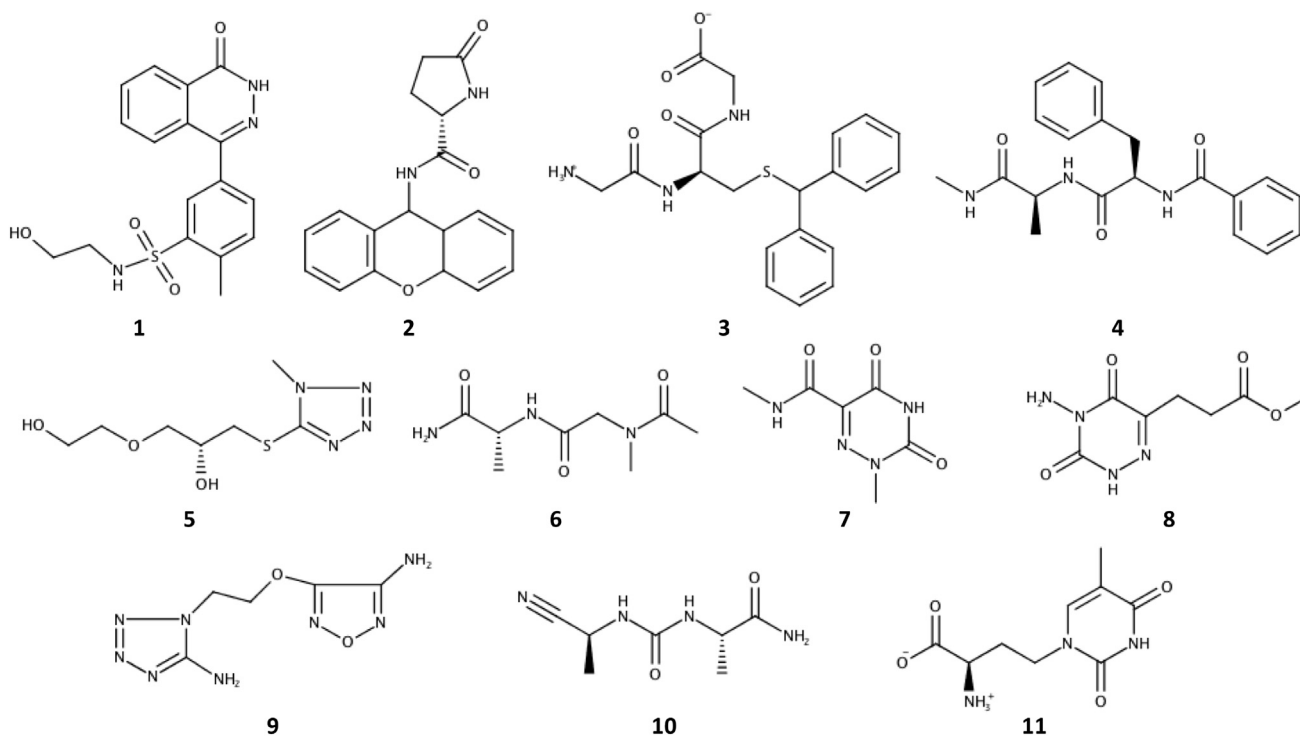


Figure 2. Small Molecules Selected as Putative Allosteric TRAP1 Ligands

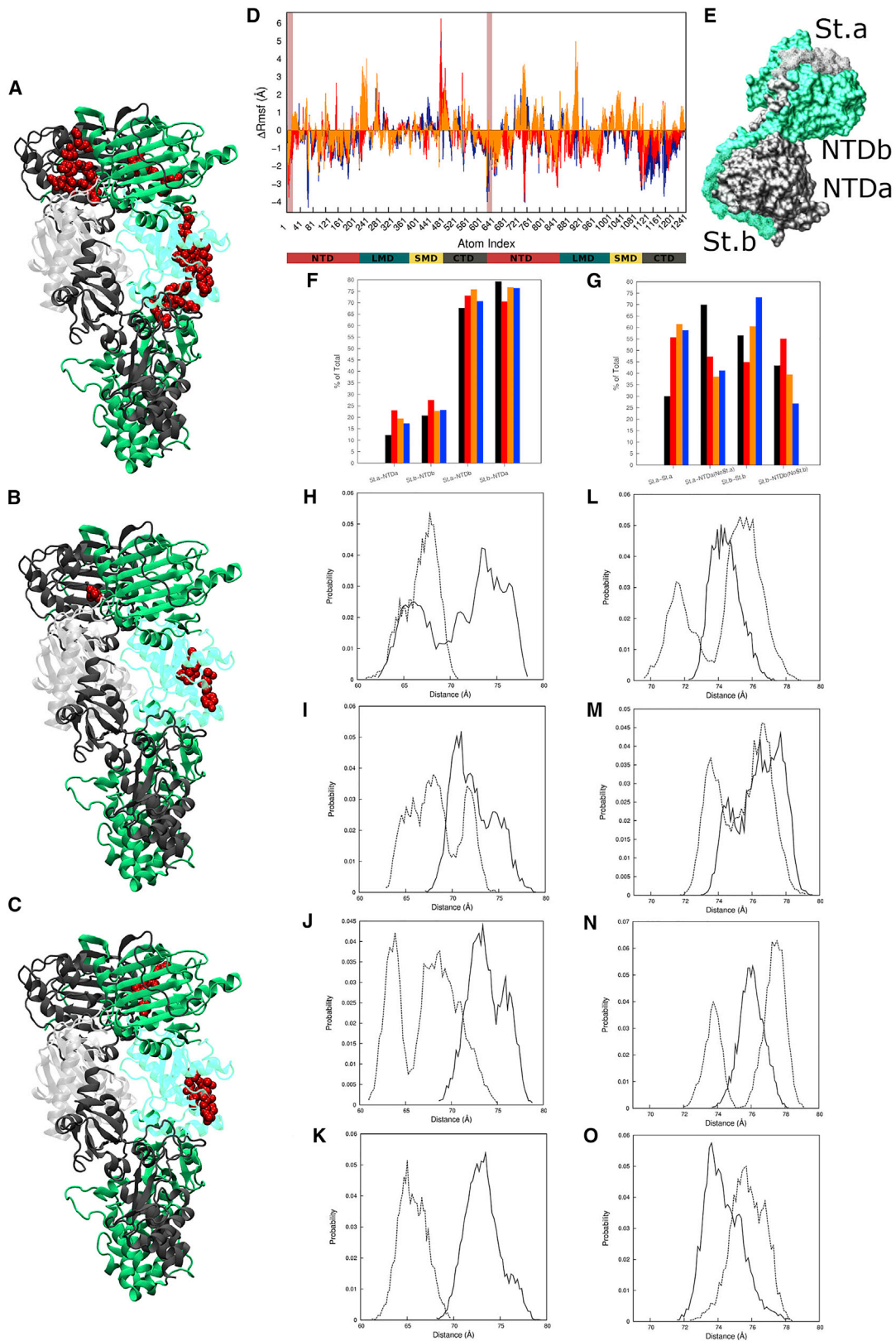
The molecular structures of the 11 molecules tested in this work.

of an aromatic cluster of residues located at the conserved hinge of motion in the three-helix bundle of the LMD whose packing/unpacking is known to regulate nucleotide-dependent conformational changes during the ATPase cycle in HSP90 family members (Morra et al., 2012; Rehn et al., 2016). Additional ligand-binding residues were located on the loop connecting helices 22 and 23, namely, Gln640, Gln641, Ala643, and Arg644. This region and adjacent residues on helix 22 define an area of asymmetry in TRAP1 that has been associated to client-chaperone interactions. Interestingly, the most active compound, 5, was the only ligand able to establish an interaction with Arg454 in cluster 3 (Figure S1). Importantly, experiments demonstrated that the distance between Arg454 and Glu699 is a viable reporter of the asymmetric state of TRAP1, indicating significant mobility for this residue during the ATPase cycle (Elnatan et al., 2017).

We then focused on the internal dynamics of the complexes via CP analysis, using the same framework as described above: namely, CP analysis was applied to filter out the regions that are consistently coordinated to the ATP site. Given the inherent flexibility of TRAP1, its allosteric site, the complexes with our ligands, and their dynamics, we did not select a single preferential binding mode to analyze the effects on TRAP1 internal dynamics. Rather, we privileged an ensemble approach whereby the ensemble of conformations sampled in the site was hypothesized to participate in determining the inhibitory effects on TRAP1 activity. In this view, the dynamic cross-talk between the protein and the ligand is explicitly considered in the analysis of their functional effects. Although the ATP-only simulations showed long-range coupling between the NTDs and the LMD

of the straight monomer (Figure 3A), allosteric ligand binding clearly interfered with such mechanisms. Compounds 5 and 7 (Figures 3B and 3C) remarkably decreased the number of preserved communicating pairs connecting the allosteric pocket with the ATP-filled catalytic site, whereas compound 6 completely abrogated long-range coordination (data not shown). The allosteric compounds thus appear to modify the dynamic coordination between the allosteric substructure, which largely overlaps with the client binding pocket and the ATP catalytic site.

Next, we calculated the overall residue-based flexibility through root-mean-square fluctuations (RMSFs) analysis of residues around their equilibrium positions. To this end, we analyzed the meta-trajectories obtained by merging the three replicates of each simulated TRAP1-inhibitor complex. RMSF is a general reporter of residue flexibility. To highlight the differences between the double ATP-TRAP1 system with or without allosteric ligand, we subtracted the RMSF values for the ATP-only state (activated state) from those obtained in each ligand-bound complex (Figure 3D). A negative value in Figure 3D thus indicates that the protein in the ATP-only state is more flexible than in the inhibitor state. A positive value indicates higher flexibility when the inhibitor is bound. The values reported in Figure 3D for the buckled (atom indexes 1–633) and the straight (atom indexes 634–1,266) monomers show that the inhibitor-bound systems are globally less flexible: this is particularly true for the N-terminal straps of the two protomers (red-shaded boxes in Figure 3D). Because straps (Figure 3E) act as important regulatory elements of TRAP1 ATPase activity, we examined the degree of coupling between the straps and the proximal NTD



(legend on next page)

regions (Figures 3F and 3G). The histograms in Figure 3F give the percentage of strap residues displaying mechanical coordination with the NTDs in each system. In the inhibitor-bound systems, both straps increased their coupling with their own NTDs, indicating a tendency for the complexes to stall the NTDs in their dimerized state. Figure 3G refers to the fraction of intra-strap-coupled residues (fragment 85–101, St.a-St.a, St.b-St.b) and to the fraction of the strap residues coupled to their cognate NTD [fragment 102–308, St.a-NTDa(NoSt.a), St.b-NTDb(NoSt.b)]; in the buckled monomer A, we once more observed a remarkable increase of strap internal coupling in the inhibitor-bound systems and a consequent reduction of the coordination involving this strap and its own NTD. The three compounds induced heterogeneous effects on the internal rigidity of the strap belonging to the straight protomer. Overall, the three inhibitors consistently increased the intra-strap and cross-domain coupling between the strap of the buckled monomer and the NTD of the straight one, decreasing global TRAP1 flexibility. In the strap of the straight protomer, the ligands caused a perturbation of coordinated motions with both NTDs. These data are once more consistent with the experimental findings of Schulze et al. (2016), who linked by fluorescence spectroscopy the conformational plasticity of the N-terminal strand of HSP90 to the acquisition of the ATPase-competent state of the chaperone.

Finally, to capture how changes in atomic fluctuations reverberate into global rearrangements within the sampled ensembles, we measured intra-/inter-monomer distances between the centers of mass of the two dynamic domains (Morra et al., 2012) consisting of the NTD and the portion including the small sub-region of the middle domain (SMD) and the whole C-terminal domain (CTD). The SMD-CTD region that hosts the allosteric ligand is responsible for client binding and structurally responds to ATP-hydrolysis in the Agard TRAP1-reactivity model (Einatan et al., 2017). The profiles of the resulting distributions are shown in Figures 3H–3O for inter- and intra-monomer NTD/SMD-CTD distances, respectively. In all cases, the presence of the inhibitors caused a perturbation in the 3D organization of TRAP1 compared with the ATP-only state. In particular, compounds 5 and 7 could push the protein toward sub-states that were not accessible to the ATP-only dimer (Figures 3H–3O). These changes in domain organization can synergistically act with the

loss of coordination between the allosteric and catalytic sites and the observed rigidification of the NTD-strap regions to perturb the conformational cycle of TRAP1.

Inhibition of the TRAP1 ATPase Cycle

We used an ATP-regenerating system on a purified human TRAP1 protein (Leskovar et al., 2008) to test the effect and selectivity of the molecules identified as putative TRAP1 allosteric inhibitors (Figure 2). We found that all compounds were able to inhibit TRAP1 ATPase activity, with some of the smallest molecules showing a degree of inhibition comparable with that of the wide-spectrum HSP90 protein family inhibitors radicicol and 17AAG, which target the catalytic site of the chaperone (Figures 4A and 4B). Importantly, in contrast with radicicol and 17AAG, most of these compounds could not achieve a significant inhibition of purified human HSP90 (Figures 4A and 4B). We chose the two most active and selective drug-like compounds, 1 and 2, and fragment-like molecules, 5–7, for further characterization. A dose-response analysis indicated that their inhibition of TRAP1 ATPase activity was superimposable to that of radicicol (Figure 4C). The dissociation constant K_D of compound 5 to TRAP1 was 288 μ M (Figure S2), as determined by surface plasmon resonance (SPR), indicating a binding affinity of the same order of magnitude as other first generation allosteric inhibitors of the HSP90 chaperone family (Roe et al., 2018; Zhao et al., 2011; Zhou et al., 2020).

These data indicate that the structure activity data of these molecules are expectedly complex, especially when comparing their activities *in vitro*, *in cellulo*, and *in vivo* (*vide infra*). Indeed, in many cases, activities and affinities for allosteric compounds have been shown not to correlate in the same direct way as those observable for orthosteric competitive inhibitors (Miyata et al., 2013; Nussinov et al., 2014)

Effect of TRAP1 Inhibition on SDH Activity

We previously demonstrated that, in tumor cells, TRAP1 down-regulates the enzymatic activity of SDH, and that 17AAG could reverse such blockade (Sciacovelli et al., 2013). SDH inhibition by TRAP1 has important biological consequences, leading to accumulation of succinate that acts as an oncometabolite and favors HIF1 α stabilization and neoplastic cell growth (Masgras et al., 2017b). Hence we used SDH activity levels to monitor

Figure 3. Effect of the Inhibitors on TRAP1 Dynamics and Long-Range Signaling

(A–C) Residues (red van der Waals sphere) that preserve long-range coordination with the ATP binding pocket of the buckled monomer A (gray) and the straight protomer B (green) are shown for the ATP-bound state alone (A), with compound 5 (B) or compound 7 (C) (see the text for residue numbering). The two dynamic domains on TRAP1 monomers (NTD and SMD-CTD) are drawn in gray (chain A) and green (chain B) with the LMD transparent.

(D) Difference RMSF plot (Δ RMSF) obtained by subtracting RMSF values of the ATP-bound from those observed in compound- and ATP-bound TRAP1 (monomer A: indexes 1–633; monomer B: indexes 634–1,266). The bar below the plot reports TRAP1 subdivision into structural domains for the two chains. In (D), (F), and (G), compound 5 is red, compound 6 is orange, and compound 7 is blue.

(E) Top view of the swapped structure of the N-terminal straps of monomers A (gray) and B (green) interacting with the NTD core of the neighboring protomer.

(F) Histograms showing the percentage of strap residues endowed with mechanical coordination with the NTD with respect to the total number of strap-connected residues (ATP-bound TRAP1: black).

(G) Histograms showing the percentages of strap residues that are internally coordinated with their own residues (St.a/b-St.a/b) and of those that are coordinated with their own NTD cores (St.a/b-NTDa/b(NoSt.a/b)).

(H–K) Inter-monomer distance distributions between the NTD of protomer A and SMD-CTD of protomer B (filled line) and between the NTD of protomer B and SMD-CTD of protomer A (dashed line) are shown for ATP-only (H), compound 5 (I), compound 6 (J), and compound 7 (K).

(L–O) Intra-monomer distance distribution between NTD and the SMD-CTD in protomer A (dashed lines) and in protomer B (filled line) for ATP (L), compound 5 (M), compound 6 (N), and compound 7 (O).

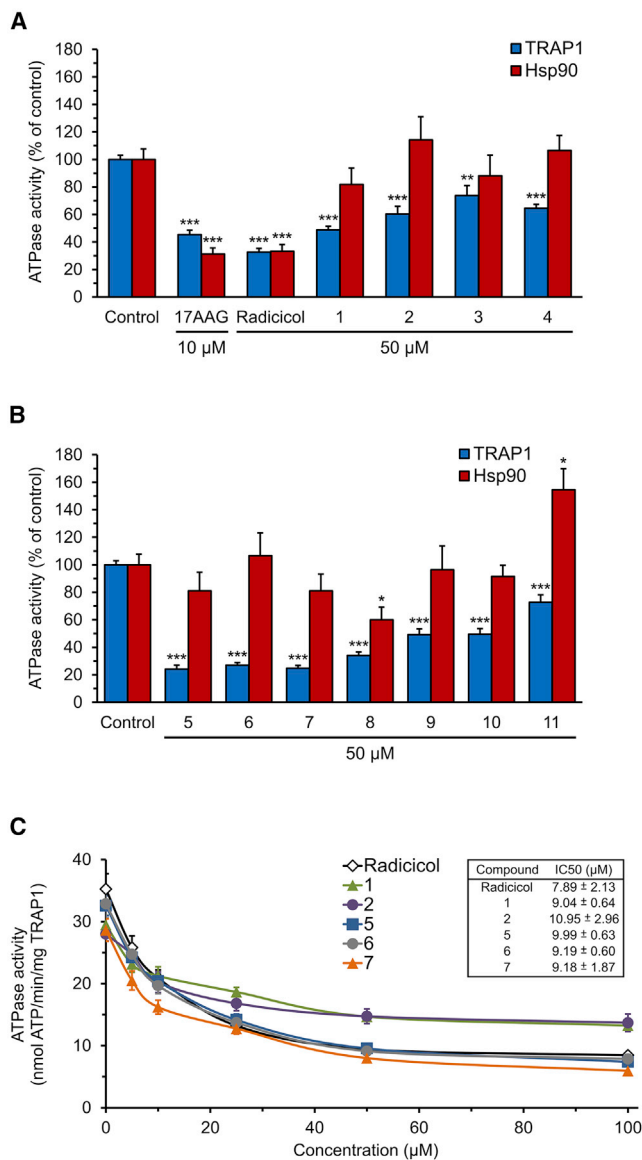


Figure 4. A Set of Putative TRAP1 Ligands Inhibits TRAP1 ATPase Activity in a Highly Selective Way

(A and B) Spectrophotometric assessment of the effects of 11 putative TRAP1 ligands (50 μ M each) on the ATPase activity of human recombinant TRAP1 or HSP90 α proteins (blue and red bars, respectively). Wide-spectrum HSP90 family inhibitors 17AAG (10 μ M) and radicicol (50 μ M) were used as positive controls.

(C) Dose-response analysis of the effect of five selected compounds on the ATPase activity of human recombinant TRAP1; radicicol was used as an inhibition control.

Mean \pm standard error of the mean (SEM) data (n = 3 independent experiments with 3 replicates for each one) are shown as normalized values with respect to vehicle-treated protein (A–C). ***p < 0.001; **p < 0.01; *p < 0.05 with an unpaired two-tailed Student's t test (A and B).

the *in cellulo* efficacy of the five selected TRAP1 allosteric inhibitors. We carried out experiments in models of malignant peripheral nerve sheath tumor (MPNST) cells, because MPNSTs are malignancies that characterize the tumor-predisposing genetic

syndrome neurofibromatosis type I (NF1) (Ratner and Miller, 2015), where we have observed that TRAP1 plays an important pro-neoplastic role (Masgras et al., 2017a). To demonstrate that TRAP1 directly interacts with SDH, we used a tripartite split-GFP approach (Cabantous et al., 2013; Koraiichi et al., 2018) co-expressing in sMPNST cells: (1) a GFP portion (GFP1–9) fused with a mitochondrial import sequence; (2) a second GFP fragment (GFP10) attached to TRAP1; and (3) the final GFP stretch, GFP11, associated with the subunit A of SDH (SDHA). Full GFP reconstitution could therefore occur only in mitochondria following direct interaction of the three portions. We found that TRAP1 binds SDHA in mitochondria (Figure 5A), and that allosteric inhibition of TRAP1 significantly reduced such interaction (Figure 5B). These experiments were carried out in TRAP1 knockout sMPNST cells, where the absence of endogenous TRAP1 does not affect SDHA protein levels (Figure 5C). We could therefore use the same cells to measure the effect of allosteric TRAP1 inhibitors on the succinate-coenzyme Q reductase (SQR) activity of SDH. All tested compounds increased SQR activity in sMPNST cells to the same extent reached following genetic ablation of TRAP1 expression or cell treatment with 17AAG (Figure 5D; Figures S3A–S3D). Enhancement of SQR activity occurred in a concentration-dependent way (Figure 5E; Figures S3A–S3D), was fast (Figures 5D–5F), long-lasting (Figure 5F), reversible upon compound removal (Figure 5G), and did not change either TRAP1 or SDHA protein levels (Figure 5H). Allosteric TRAP1 inhibitors were similarly effective on SQR activity of SDH in other mouse and human MPNST cell types (Figures S3E–S3J).

Biological Effects of TRAP1 Allosteric Inhibitors

We then investigated whether TRAP1 inhibition could influence any cellular biological routine. None of the five selected molecules was able per se to induce death in the cell models that we tested, which were instead sensitive to 17AAG-induced toxicity (Figure 6A; Figures S4A–S4C). Nonetheless, the cell proliferation rate was slightly decreased in TRAP1 knockout cells, and this deceleration was fully mimicked by allosteric inhibitors of TRAP1 (Figure 6B; Figures S4D–S4F). In the case of compound 1, we measured a marked inhibition of cell proliferation independently of TRAP1 expression (Figure 6B), indicating that this was an off-target effect; hence compound 1 was excluded from further analyses.

We have previously observed that TRAP1-dependent inhibition of SDH is enhanced when cells are placed under stress conditions that mimic those encountered during tumor growth (Sciacovelli et al., 2013), and that TRAP1 activity is required for *in vitro* tumorigenic growth of diverse cell models (Masgras et al., 2017a; Sciacovelli et al., 2013). Therefore, we evaluated the effect of TRAP1 allosteric inhibition on an *in vitro* experiment of tumorigenesis. We found that mouse sMPNST cells readily overcame contact inhibition and formed foci, thus confirming their tumorigenicity, and this was abrogated by knocking out TRAP1 expression (Figures 6C and 6D). Consistently, TRAP1-targeting molecules completely ablated formation of foci, even at the lowest concentrations that we tested (Figures 6C–6F).

Finally, we analyzed the *in vivo* effect of TRAP1 allosteric inhibition. To this aim, we used a morpholino approach

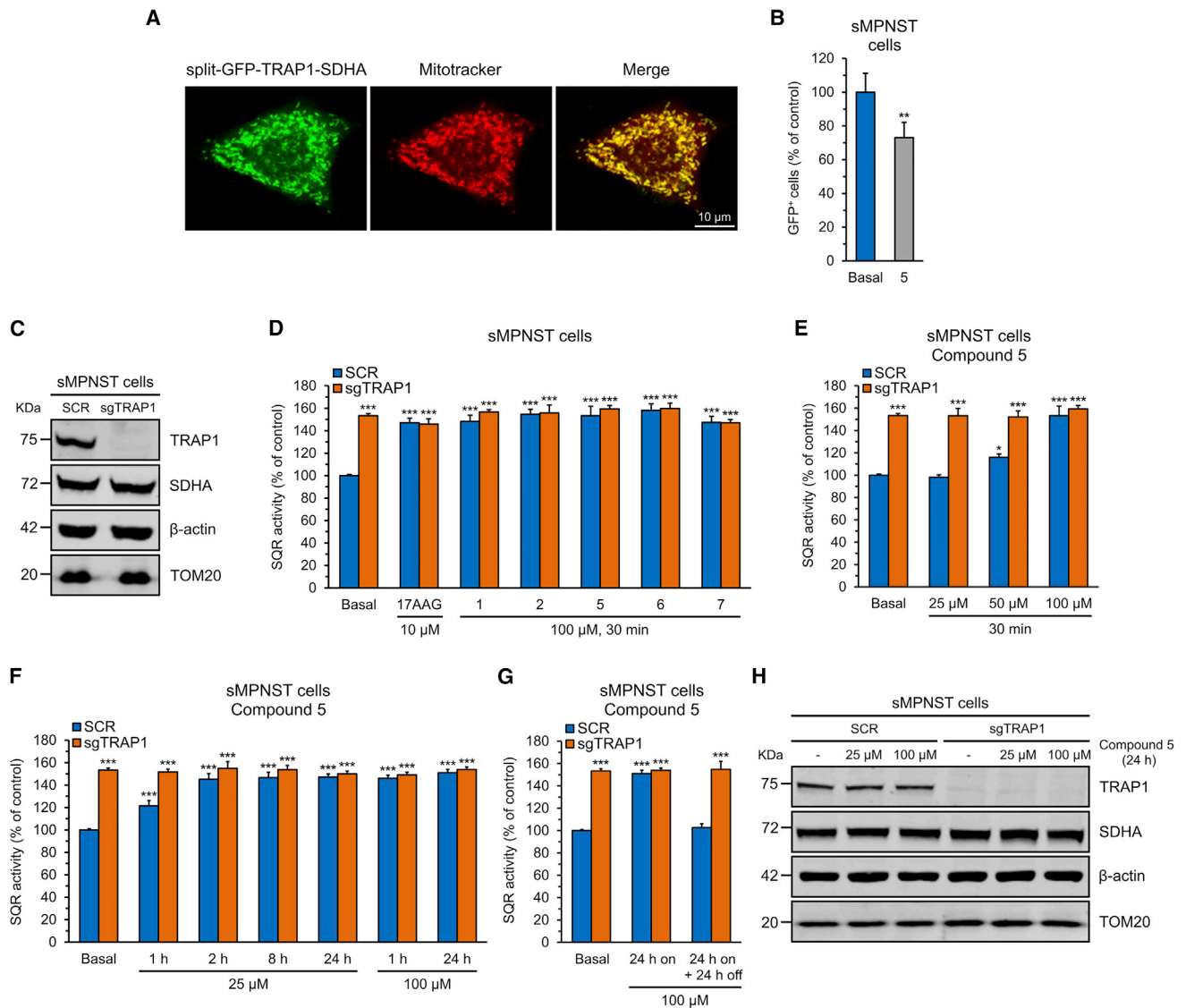


Figure 5. TRAP1 Inhibition Increases SDH Enzymatic Activity

(A) Representative tripartite split GFP experiment on cells co-transfected with GFP11-9 fused with a mitochondrial import sequence, GFP10-TRAP1 and GFP11-SDHA. Green dots indicate mitochondrial interaction between TRAP1 and SDHA. MitoTracker (red dots) was used to stain mitochondria; superimposition of MitoTracker and GFP signal is shown as yellow dots.

(B) Quantification of GFP-positive cells with or without compound 5 (100 μ M, 48 h). Data are presented as mean \pm SEM, n = 636 individual positive control cells and n = 725 individual positive treated cells from four independent replicates; **p < 0.01 with a paired two-tailed Student's t test.

(C) Ablation of TRAP1 expression by a single guide RNA (sgTRAP1) with the CRISPR/Cas9 technology (SCR: cells expressing a scrambled guide RNA) did not change SDHA protein levels.

(D–G) Spectrophotometric analysis of the succinate-coenzyme Q reductase (SQR) activity of SDH on intact cells. (D) Cells were treated with the same panel of compounds of Figure 4C (100 μ M each), (E) dose-response analysis of a 30-min cell exposure to compound 5, and (F and G) kinetics analysis of the effect of compound 5. In (G), “off” indicates compound removal from culture medium. In (D)–(G), data are presented as mean \pm SEM (n = 3 independent experiments with 3 replicates for each one); ***p < 0.001; *p < 0.05 with one-way ANOVA with post hoc Bonferroni's test.

(H) TRAP1 expression levels in cells treated with compound 5 (25 and 100 μ M, 24 h).

In (C) and (H), actin and TOM20 were used as cytosol and mitochondria loading controls, respectively. (A–H) Experiments were carried out on sMPNST cells.

(Nasevicius and Ekker, 2000) for knocking down TRAP1 expression in whole larvae of zebrafish (*Danio rerio*) (Figure 6G). We found that supply of compound 5 in the fish water increased SDH enzymatic activity of wild-type larvae to the

same level measured in animals without TRAP1. This was a specific effect, because the allosteric inhibitor of TRAP1 was ineffective on the SDH activity of TRAP1 morpholino animals (Figure 6H).

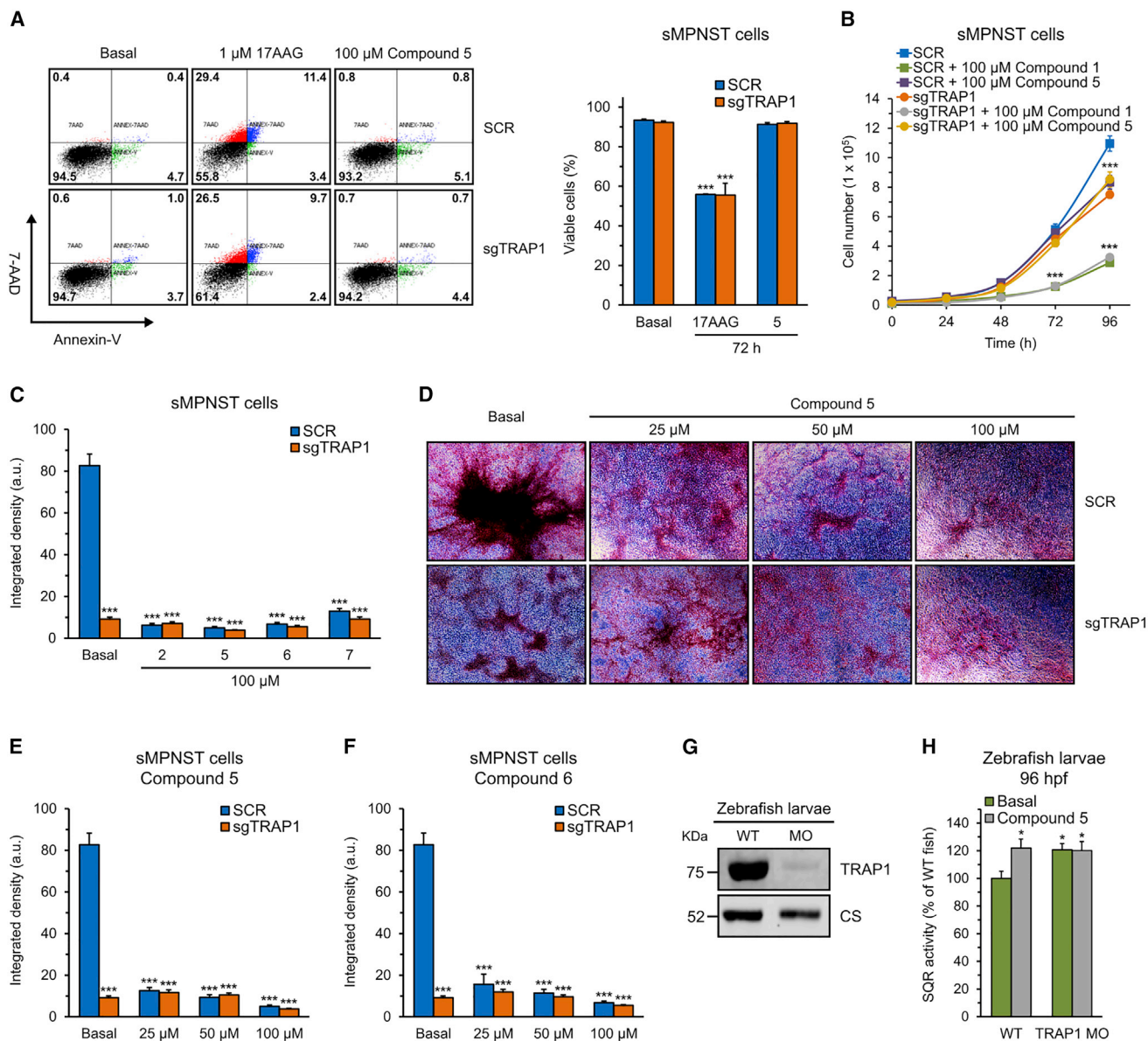


Figure 6. In Cellulo and In Vivo Effects of Allosteric TRAP1 Inhibitors

(A) Viability of cells treated with either 17AAG (1 μ M) or compound 5 (100 μ M) for 72 h. On the left, representative traces of cytofluorimetric analyses; green: Annexin V-fluorescein isothiocyanate (FITC)-positive, early apoptotic cells; red: 7-aminoactinomycin D (7-AAD)-positive, necrotic cells; blue: Annexin V-FITC/7-AAD double-positive, late apoptotic cells; black: double-negative, viable cells. The percentage of each cell subpopulation is reported. On the right, bar graph quantification of cell viability.

(B) Effects of compounds 1 and 5 (100 μ M each, 96 h) on cell proliferation.

(C–F) Focus-forming assay on cells grown for 10 days with or without selective TRAP1 inhibitors. Foci are quantified using an integrated density parameter that evaluates both their surface and thickness. (C) Effect of compounds 2, 5, 6, and 7 (100 μ M each) on focus growth; (D) representative pictures of foci formed with or without the reported concentrations of compound 5; and (E and F) dose-response analysis of the effect of compounds 5 and 6, respectively, on focus growth. (A–C, E, and F) Data are presented as mean \pm SEM (n = 3 independent experiments with 3 replicates for each one); ***p < 0.001 with one-way ANOVA with post hoc Bonferroni's test. All experiments were carried out on sMPNST cells with or without TRAP1 (SCR and sgTRAP1, respectively).

(G) TRAP1 expression level in zebrafish (*Danio rerio*) larvae 96 h post-fertilization (hpf), either wild type or injected with a morpholino (MO) against zebrafish TRAP1. The mitochondrial protein citrate synthase (CS) was used as a loading control.

(H) Spectrophotometric analysis of the SQR activity of SDH on wild-type and MO zebrafish larvae treated with compound 5 (100 μ M, 4 h). Data are presented as mean \pm SEM (n = 4 independent experiments, with 60 fishes used in each experiment); *p < 0.05 with one-way ANOVA with post hoc Bonferroni's test.

DISCUSSION

In this work, we have reported the rational, structure-based, and dynamics-based discovery of ligands selective for TRAP1 targeting. These molecules can be used to investigate the complex biology of the chaperone and further evolved into leads for the treatment of diseases in which TRAP1 plays a key role. Our results demonstrate that the explicit consideration of the internal, functionally oriented dynamics of TRAP1 can unveil specific allosteric pockets, distal from the highly conserved ATP-binding site and characterized by structural and chemical features that are distinct from those of other paralogs of the HSP90 family (Ferraro et al., 2019; Moroni et al., 2018).

Allostery is one of the prime mechanisms that underpin fine conformational regulation: ligand binding (or covalent modification) at one site can modify the structural dynamic properties of the protein, modulating affinity toward a primary binding event or reactivity toward a substrate at the distal binding/catalytic site. Allosteric binding shifts the population of ensembles that determine biological activities. The final result is the perturbation of the functionally relevant dynamic modes, which in turn reverberates in an increase or decrease of protein activity and its downstream effects in the cell. Understanding the chemical determinants of allosteric recognition and their consequences on the functions of TRAP1 is an essential requirement to design new chemical entities, with the aim of testing mechanistic ideas and comparing *in vitro* and *in vivo* behavior.

Here, we used the structural, dynamic, and chemical features of the putative TRAP1 allosteric pocket to unveil the functional requirements necessary for small molecules to bind. The integrated analysis of protein structure and dynamics is thus the basis for selective allosteric inhibition. After experimental validation of the selective effects of discovered molecules *in vitro* and *in vivo*, we use atomistic simulations to provide a structure- and dynamics-based model of allosteric perturbation. In this framework, binding at the allosteric hotspot impacts on TRAP1 functions by perturbing the dynamic coupling mechanisms between the M-domain and ATP binding/hydrolysis. The allosteric site largely overlaps the region that undergoes structural rearrangements during ATP hydrolysis and client binding/remodeling. Allosteric inhibitors disrupt this functional coupling and modify the conformational dynamics of TRAP1, favoring an ensemble of states where the protein is stalled in the NTD-dimerized state and slowing down the dynamics of the chaperone cycle, which ultimately reverberates in functional perturbation. One additional advantage of allosteric inhibitors, which could in principle extend to the whole HSP90 family, is their potential to escape naturally occurring resistance mechanisms observed against ATP-competitive inhibitors (Millson et al., 2011; Prodromou et al., 2009). Subtle structural mutations around the catalytic pocket have been shown to reduce affinity for the competitive inhibitors, while preserving ATP recognition and catalytic efficiency. Because distal (cryptic) allosteric sites are under lower evolutionary pressure than catalytic sites, mutation-based resistance mechanisms may expectedly have lower impact on the viability of allosteric modulators.

It is worth noting that our approach is based on the use of the experimental high-resolution X-ray structure of the ATP-bound, closed conformation of TRAP1, which aptly represents the activated state of the protein. The dynamic nature of TRAP1 expectedly permits the protein to undergo large-scale rearrangements and explore alternative conformations (as well as nucleotide states) during its chaperone cycle. In this scenario, our model hypothesizes that the allosteric molecules likely bind a subset of (activated) TRAP1 molecules at any given time, sufficient to perturb its functions. As a caveat, it should be underlined that alternative, partially closed or even open conformations are present at equilibrium and could be targeted by the ligands. The ligands would thus act by either moving the equilibrium away from the TRAP1 active state or by blocking the motions that determine either the opening or the closing of the protomers. These two hypotheses are not incompatible, and indeed a combination of the two scenarios is likely an appropriate mechanistic explanation. However, the atomistic characterization of the functionally oriented large-scale conformational changes of TRAP1 is still out of reach both for plain MD simulations, due to the sheer dimensions of the system, and for enhanced sampling methods, due to the difficulties of defining appropriate collective variables that recapitulate the complex motions involved in the chaperone cycle, including protomer opening, domain rotations, and strap detachment and reorganization. The investigation of how changes on a short time scale, starting from the experimentally available catalytic state, may reverberate in the modulation of the slow motions of regions that determine biological functions could be corroborated by novel spectroscopic approaches (Schulze et al., 2016) that shed light on the relevance of rapid protein dynamics in modulating intra- and inter-domain interactions.

Although successful examples of modification of known ATP-competitive inhibitors to improve selectivity for a certain HSP90 isoform have been reported (Khandelwal et al., 2018; Patel et al., 2013; Zhao et al., 2015), including the use of mitochondrial delivery vehicles to reach TRAP1 (Lee et al., 2015; Park et al., 2017), our approach is the first that rationally exploits TRAP1 asymmetry to discover binding sites alternative to the ATP binding site. Furthermore, the use of a pharmacophore model derived from the conformational sampling of the active state of the receptor permits exploring a wide portion of chemical space, expanding the diversity of the predicted ligands and avoiding the constraints generally associated with the modification of defined chemical scaffolds. Importantly, the selected molecules display highly selective, dose-dependent inhibition of TRAP1 ATPase activity, while leaving cytosolic HSP90 unperturbed. In this context, it is important to underline that the peculiar asymmetric features of the discovered TRAP1 allosteric site make it distinct from the allosteric sites identified for HSP90 at the borders between SMD and CTD domains. Although the TRAP1 allosteric site is fully localized on the straight protomer (see Figure 1A), in general HSP90 allosteric binding sites are symmetric and located in a region between the two protomers (Ferraro et al., 2019; Roe et al., 2018; Sattin et al., 2015; Zhao et al., 2015) (see Figure S5 showing the differences in structure and dynamics, which are already described in Moroni et al., 2018), between allosteric sites in TRAP1 and cytosolic HSP90).

The selection of new paralog-selective inhibitors of TRAP1 may be important for both fundamental and applicative reasons. From the fundamental point of view, although it is largely appreciated that the various isoforms of HSP90 (HSP90 α , HSP90 β , Grp94, and TRAP1) play different roles in the biology of the cell, partly because of their differential subcellular localization, the specific functions of each paralog have not been fully clarified. A thorough and detailed dissection of the biochemical circuitries tuned by the chaperone activity of each paralog is instrumental to comprehend how dysfunctions of these pathways influence the pathogenesis of various diseases, ranging from cancer to neurodegeneration and inflammation.

Small molecules, like the ones that we have discovered and characterized here, can be used to selectively block the functions of TRAP1 in conditions where it is overexpressed, as observed in different tumor types and grades (Rasola et al., 2014). In addition, TRAP1 activity can be regulated in subtle and flexible modes via post-translational modifications, which influence client activity and subsequent biochemical and biological responses. Indeed, TRAP1 modulates cell tumorigenicity following interaction with the kinases Src and extracellular signal-regulated kinases 1 and 2 (ERK1/2) and the ensuing inhibition of cytochrome c oxidase and SDH, respectively (Masgras et al., 2017a; Yoshida et al., 2013), as well as after its SIRT3-dependent deacetylation (Park et al., 2019). In turn, TRAP1 stabilizes these kinases and deacetylases in mitochondria, even under stress conditions, and this probably radiates further biochemical effects that need to be disentangled and related to specific environmental conditions. The availability of chemical tools that selectively perturb the functions of TRAP1 in a controlled manner permits illumination of the biological consequences of such perturbation. This can be studied in the native cellular environment under specific biochemical states, such as (de)phosphorylation and/or (de)acetylation, and pathophysiological conditions that span from changes in nutrient or oxygen availability to cancer, degenerative disorders, and ischemic states.

From the applicative point of view, the selective inhibition of the functions of TRAP1, possibly without interference with other HSP90 functions, could have a positive effect on the treatment of disorders that are strictly dependent on TRAP1, avoiding the problems connected with the heat shock response observed upon using pan-HSP90 inhibitors. In this framework, blocking TRAP1 by chemical inhibition can be potentially used for therapeutic intervention. The molecules unveiled here represent viable starting points for the development of novel leads with optimized pharmacological profiles.

STAR★METHODS

Detailed methods are provided in the online version of this paper and include the following:

- **KEY RESOURCES TABLE**
- **LEAD CONTACTS AND MATERIAL AVAILABILITY**
- **EXPERIMENTAL MODEL AND SUBJECT DETAILS**
 - Mouse and Human MPNST cell lines
 - Animals

● **METHOD DETAILS**

- Initial Molecular Dynamics Simulations of ATP-bound TRAP1
- Computational identification of allosteric pockets
- Pharmacophore development and virtual screening
- Molecular Dynamics simulations of the allosteric inhibitor-bound TRAP1 complexes
- Long- and short-range communication analysis of the allosteric inhibitor-bound TRAP1 complexes
- Cluster analysis of ligand conformations
- Production and purification of recombinant human TRAP1
- Measurement of TRAP1 and Hsp90 ATPase activities
- Measurement of kinetic constants with surface plasmon resonance (SPR)
- Generation of TRAP1 knock-out MPNST cell lines
- Knockdown of TRAP1 in wild-type zebrafish embryos
- TRAP1-SDHA interaction assays
- Cell fractionation and immunoblotting
- Measurement of succinate:coenzyme Q reductase (SQR) activity of succinate dehydrogenase (SDH)
- Cell viability assays
- Cell proliferation assays
- *In vitro* tumorigenesis assays

● **QUANTIFICATION AND STATISTICAL ANALYSIS**

● **DATA AND CODE AVAILABILITY**

SUPPLEMENTAL INFORMATION

Supplemental Information can be found online at <https://doi.org/10.1016/j.celrep.2020.107531>.

ACKNOWLEDGMENTS

A.R. was supported by grants from University of Padova, Neurofibromatosis Therapeutic Acceleration Program, Associazione Italiana Ricerca Cancro (AIRC grant IG 2017/20749), Children's Tumor Foundation Drug Discovery Initiative (award grant 2016A-05-009), and Piano for Life Onlus and Linfa OdV. I.M. was recipient of a Young Investigator Award Grant from Children's Tumor Foundation. G. Colombo was supported by grants from Associazione Italiana Ricerca Cancro (AIRC grant IG 2017/20019) and Neurofibromatosis Therapeutic Acceleration Program. We thank David Agard, UCSF, for providing the pET151/D-TOPO/TRAP1 plasmid and Elena Trevisan for inextinguishable technical support.

AUTHOR CONTRIBUTIONS

Conceptualization: G. Colombo and A.R.; Investigation: C.S.-M., E.M., M.F., C.L., G. Cannino, I.M., and A.N.; Resources: A.N. and P.Q.; Formal Analysis: C.S.-M., E.M., and M.F.; Visualization: C.S.-M., E.M., and M.F.; Funding Acquisition: G. Colombo and A.R.; Supervision: G. Cannino and A.R.; Project Administration: G. Cannino and A.R.; Writing – Original Draft: G. Colombo and A.R.; Writing – Review & Editing: C.S.-M., E.M., M.F., G. Colombo, and A.R.

DECLARATION OF INTERESTS

The authors declare no competing interests.

Received: October 10, 2019

Revised: February 28, 2020

Accepted: March 27, 2020

Published: April 21, 2020

REFERENCES

- Amoroso, M.R., Matassa, D.S., Agliarulo, I., Avolio, R., Lu, H., Sisinni, L., Lettini, G., Gabra, H., Landriscina, M., and Esposito, F. (2016). TRAP1 downregulation in human ovarian cancer enhances invasion and epithelial-mesenchymal transition. *Cell Death Dis.* **7**, e2522.
- Bernardi, P., Rasola, A., Forte, M., and Lippe, G. (2015). The Mitochondrial Permeability Transition Pore: Channel Formation by F-ATP Synthase, Integration in Signal Transduction, and Role in Pathophysiology. *Physiol. Rev.* **95**, 1111–1155.
- Butler, E.K., Voigt, A., Lutz, A.K., Toegel, J.P., Gerhardt, E., Karsten, P., Falckenburger, B., Reinartz, A., Winkhofer, K.F., and Schulz, J.B. (2012). The mitochondrial chaperone protein TRAP1 mitigates α -Synuclein toxicity. *PLoS Genet.* **8**, e1002488.
- Cabantous, S., Nguyen, H.B., Pedelacq, J.D., Koraïchi, F., Chaudhary, A., Ganguly, K., Lockard, M.A., Favre, G., Terwilliger, T.C., and Waldo, G.S. (2013). A new protein-protein interaction sensor based on tripartite split-GFP association. *Sci. Rep.* **3**, 2854.
- Case, D.A., Cerutti, D.S., Cheatham, T.E.I., Darden, T.A., Duke, R.E., Giese, T.J., Gohlke, H., Goetz, A.W., Greene, D., Homeyer, N., et al. (2017). AMBER 2017 (University of California, San Francisco).
- Ciscato, F., Sciacovelli, M., Villano, G., Turato, C., Bernardi, P., Rasola, A., and Pontisso, P. (2014). SERPINB3 protects from oxidative damage by chemotherapeutics through inhibition of mitochondrial respiratory complex I. *Oncotarget* **5**, 2418–2427.
- Costa, A.C., Loh, S.H., and Martins, L.M. (2013). Drosophila Trap1 protects against mitochondrial dysfunction in a PINK1/parkin model of Parkinson's disease. *Cell Death Dis.* **4**, e467.
- Darden, T., York, D., and Pedersen, L. (1993). Particle mesh Ewald: An $N \cdot \log(M)$ method for Ewald sums in large systems. *J. Chem. Phys.* **98**, 10089.
- Daura, X., Gademann, K., Jaun, B., Seebach, D., van Gunsteren, W.F., and Mark, A.E. (1999). Peptide folding: when simulation meets experiment. *Angew. Chem. Int.* **38**, 236–240.
- Elnatan, D., Betegon, M., Liu, Y., Ramelot, T., Kennedy, M.A., and Agard, D.A. (2017). Symmetry broken and rebroken during the ATP hydrolysis cycle of the mitochondrial Hsp90 TRAP1. *eLife* **6**, e25235.
- Ferraro, M., D'Annessa, I., Moroni, E., Morra, G., Paladino, A., Rinaldi, S., Compostella, F., and Colombo, G. (2019). Allosteric Modulators of HSP90 and HSP70: Dynamics Meets Function through Structure-Based Drug Design. *J. Med. Chem.* **62**, 60–87.
- Fitzgerald, J.C., Zimprich, A., Carvajal Berrio, D.A., Schindler, K.M., Maurer, B., Schulte, C., Bus, C., Hauser, A.K., Kübler, M., Lewin, R., et al. (2017). Metformin reverses TRAP1 mutation-associated alterations in mitochondrial function in Parkinson's disease. *Brain* **140**, 2444–2459.
- Guzzo, G., Sciacovelli, M., Bernardi, P., and Rasola, A. (2014). Inhibition of succinate dehydrogenase by the mitochondrial chaperone TRAP1 has anti-oxidant and anti-apoptotic effects on tumor cells. *Oncotarget* **5**, 11897–11908.
- Jorgensen, W.L., Chandrasekhar, J., Madura, J.D., Impey, R.W., and Klein, M.L. (1983). Comparison of simple potential functions for simulating liquid water. *J. Chem. Phys.* **79**, 926–935.
- Karagöz, G.E., and Rüdiger, S.G. (2015). Hsp90 interaction with clients. *Trends Biochem. Sci.* **40**, 117–125.
- Khandelwal, A., Kent, C.N., Balch, M., Peng, S., Mishra, S.J., Deng, J., Day, V.W., Liu, W., Subramanian, C., Cohen, M., et al. (2018). Structure-guided design of an Hsp90 β N-terminal isoform-selective inhibitor. *Nat. Commun.* **9**, 425.
- Kimmel, C.B., Ballard, W.W., Kimmel, S.R., Ullmann, B., and Schilling, T.F. (1995). Stages of embryonic development of the zebrafish. *Dev. Dyn.* **203**, 253–310.
- Koraïchi, F., Gence, R., Bouchenot, C., Grosjean, S., Lajoie-Mazenc, I., Favre, G., and Cabantous, S. (2018). High-content tripartite split-GFP cell-based assays to screen for modulators of small GTPase activation. *J. Cell Sci.* **131**, jcs210419.
- Kowalik, M.A., Guzzo, G., Morandi, A., Perra, A., Menegon, S., Masgras, I., Trevisan, E., Angioni, M.M., Fornari, F., Quagliata, L., et al. (2016). Metabolic reprogramming identifies the most aggressive lesions at early phases of hepatic carcinogenesis. *Oncotarget* **7**, 32375–32393.
- Lavery, L.A., Partridge, J.R., Ramelot, T.A., Elnatan, D., Kennedy, M.A., and Agard, D.A. (2014). Structural asymmetry in the closed state of mitochondrial Hsp90 (TRAP1) supports a two-step ATP hydrolysis mechanism. *Mol. Cell* **53**, 330–343.
- Lee, C., Park, H.K., Jeong, H., Lim, J., Lee, A.J., Cheon, K.Y., Kim, C.S., Thomas, A.P., Bae, B., Kim, N.D., et al. (2015). Development of a mitochondria-targeted Hsp90 inhibitor based on the crystal structures of human TRAP1. *J. Am. Chem. Soc.* **137**, 4358–4367.
- Leskovaar, A., Wegele, H., Werbeck, N.D., Buchner, J., and Reinstein, J. (2008). The ATPase cycle of the mitochondrial Hsp90 analog Trap1. *J. Biol. Chem.* **283**, 11677–11688.
- Lindorff-Larsen, K., Piana, S., Palmo, K., Maragakis, P., Klepeis, J.L., Dror, R.O., and Shaw, D.E. (2010). Improved side-chain torsion potentials for the Amber ff99SB protein force field. *Proteins* **78**, 1950–1958.
- Masgras, I., Ciscato, F., Brunati, A.M., Tibaldi, E., Indraccolo, S., Curtarello, M., Chiara, F., Cannino, G., Papaleo, E., Lambrughini, M., et al. (2017a). Absence of Neurofibromin Induces an Oncogenic Metabolic Switch via Mitochondrial ERK-Mediated Phosphorylation of the Chaperone TRAP1. *Cell Rep.* **18**, 659–672.
- Masgras, I., Sanchez-Martin, C., Colombo, G., and Rasola, A. (2017b). The Chaperone TRAP1 As a Modulator of the Mitochondrial Adaptations in Cancer Cells. *Front. Oncol.* **7**, 58.
- Millson, S.H., Chua, C.-S., Roe, S.M., Polier, S., Solovieva, S., Pearl, L.H., Sim, T.-S., Prodromou, C., and Piper, P.W. (2011). Features of the Streptomyces hygrosopicus HtpG reveal how partial geldanamycin resistance can arise with mutation to the ATP binding pocket of a eukaryotic Hsp90. *FASEB J.* **25**, 3828–3837.
- Miyamoto, S., and Kollman, P.A. (1992). SETTLE: an analytical version of the SHAKE and RATTLE algorithm for rigid water models. *J. Comput. Chem.* **13**, 952–962.
- Miyata, Y., Li, X., Lee, H.-F., Jinwal, U.K., Srinivasan, S.R., Seguin, S.P., Young, Z.T., Brodsky, J.L., Dickey, C.A., Sun, D., and Gestwicki, J.E. (2013). Synthesis and initial evaluation of YM-08, a blood-brain barrier permeable derivative of the heat shock protein 70 (Hsp70) inhibitor MKT-077, which reduces tau levels. *ACS Chem. Neurosci.* **4**, 930–939.
- Mo, W., Chen, J., Patel, A., Zhang, L., Chau, V., Li, Y., Cho, W., Lim, K., Xu, J., Lazar, A.J., et al. (2013). CXCR4/CXCL12 mediate autocrine cell-cycle progression in NF1-associated malignant peripheral nerve sheath tumors. *Cell* **152**, 1077–1090.
- Moroni, E., Agard, D.A., and Colombo, G. (2018). The Structural Asymmetry of Mitochondrial Hsp90 (Trap1) Determines Fine Tuning of Functional Dynamics. *J. Chem. Theory Comput.* **14**, 1033–1044.
- Morra, G., Potestio, R., Micheletti, C., and Colombo, G. (2012). Corresponding functional dynamics across the Hsp90 Chaperone family: insights from a multi-scale analysis of MD simulations. *PLoS Comput. Biol.* **8**, e1002433.
- Nasevicius, A., and Ekker, S.C. (2000). Effective targeted gene 'knockdown' in zebrafish. *Nat. Genet.* **26**, 216–220.
- Nussinov, R., Tsai, C.-J., and Liu, J. (2014). Principles of allosteric interactions in cell signaling. *J. Am. Chem. Soc.* **136**, 17692–17701.
- Park, H.K., Jeong, H., Ko, E., Lee, G., Lee, J.E., Lee, S.K., Lee, A.J., Im, J.Y., Hu, S., Kim, S.H., et al. (2017). Paralog Specificity Determines Subcellular Distribution, Action Mechanism, and Anticancer Activity of TRAP1 Inhibitors. *J. Med. Chem.* **60**, 7569–7578.
- Park, H.K., Hong, J.H., Oh, Y.T., Kim, S.S., Yin, J., Lee, A.J., Chae, Y.C., Kim, J.H., Park, S.H., Park, C.K., et al. (2019). Interplay between TRAP1 and Sirtuin-3 Modulates Mitochondrial Respiration and Oxidative Stress to Maintain Stemness of Glioma Stem Cells. *Cancer Res.* **79**, 1369–1382.
- Patel, P.D., Yan, P., Seidler, P.M., Patel, H.J., Sun, W., Yang, C., Que, N.S., Taldone, T., Finotti, P., Stephani, R.A., et al. (2013). Paralog-selective Hsp90

- inhibitors define tumor-specific regulation of HER2. *Nat. Chem. Biol.* **9**, 677–684.
- Prodromou, C., Nuttall, J.M., Millson, S.H., Roe, S.M., Sim, T.-S., Tan, D., Workman, P., Pearl, L.H., and Piper, P.W. (2009). Structural basis of the radical resistance displayed by a fungal hsp90. *ACS Chem. Biol.* **4**, 289–297.
- Rasola, A., Neckers, L., and Picard, D. (2014). Mitochondrial oxidative phosphorylation TRAP(1)ped in tumor cells. *Trends Cell Biol.* **24**, 455–463.
- Ratner, N., and Miller, S.J. (2015). A RASopathy gene commonly mutated in cancer: the neurofibromatosis type 1 tumour suppressor. *Nat. Rev. Cancer* **15**, 290–301.
- Rehn, A., Moroni, E., Zierer, B.K., Tippel, F., Morra, G., John, C., Richter, K., Colombo, G., and Buchner, J. (2016). Allosteric Regulation Points Control the Conformational Dynamics of the Molecular Chaperone Hsp90. *J. Mol. Biol.* **428**, 4559–4571.
- Roe, M.S., Wahab, B., Török, Z., Horváth, I., Vigh, L., and Prodromou, C. (2018). Dihydropyridines Allosterically Modulate Hsp90 Providing a Novel Mechanism for Heat Shock Protein Co-induction and Neuroprotection. *Front. Mol. Biosci.* **5**, 51.
- Sanjana, N.E., Shalem, O., and Zhang, F. (2014). Improved vectors and genome-wide libraries for CRISPR screening. *Nat. Methods* **11**, 783–784.
- Sattin, S., Tao, J., Vettoretti, G., Moroni, E., Pennati, M., Lopergolo, A., Morelli, L., Bugatti, A., Zuehlke, A., Moses, M., et al. (2015). Activation of Hsp90 Enzymatic Activity and Conformational Dynamics through Rationally Designed Allosteric Ligands. *Chemistry* **21**, 13598–13608.
- Schopf, F.H., Biebl, M.M., and Buchner, J. (2017). The HSP90 chaperone machinery. *Nat. Rev. Mol. Cell Biol.* **18**, 345–360.
- Schulze, A., Beliu, G., Helmerich, D.A., Schubert, J., Pearl, L.H., Prodromou, C., and Neuweiler, H. (2016). Cooperation of local motions in the Hsp90 molecular chaperone ATPase mechanism. *Nat. Chem. Biol.* **12**, 628–635.
- Sciacovelli, M., Guzzo, G., Morello, V., Frezza, C., Zheng, L., Nannini, N., Calabrese, F., Laudiero, G., Esposito, F., Landriscina, M., et al. (2013). The mitochondrial chaperone TRAP1 promotes neoplastic growth by inhibiting succinate dehydrogenase. *Cell Metab.* **17**, 988–999.
- Semenza, G.L. (2013). HIF-1 mediates metabolic responses to intratumoral hypoxia and oncogenic mutations. *J. Clin. Invest.* **123**, 3664–3671.
- Shrestha, L., Bolaender, A., Patel, H.J., and Taldone, T. (2016). Heat Shock Protein (HSP) Drug Discovery and Development: Targeting Heat Shock Proteins in Disease. *Curr. Top. Med. Chem.* **16**, 2753–2764.
- Spyra, M., Kluwe, L., Hagel, C., Nguyen, R., Panse, J., Kurtz, A., Mautner, V.F., Rabkin, S.D., and Demestre, M. (2011). Cancer stem cell-like cells derived from malignant peripheral nerve sheath tumors. *PLoS ONE* **6**, e21099.
- Taipale, M., Jarosz, D.F., and Lindquist, S. (2010). HSP90 at the hub of protein homeostasis: emerging mechanistic insights. *Nat. Rev. Mol. Cell Biol.* **11**, 515–528.
- Vogel, K.S., Klesse, L.J., Velasco-Miguel, S., Meyers, K., Rushing, E.J., and Parada, L.F. (1999). Mouse tumor model for neurofibromatosis type 1. *Science* **286**, 2176–2179.
- Voloboueva, L.A., Duan, M., Ouyang, Y., Emery, J.F., Stoy, C., and Giffard, R.G. (2008). Overexpression of mitochondrial Hsp70/Hsp75 protects astrocytes against ischemic injury in vitro. *J. Cereb. Blood Flow Metab.* **28**, 1009–1016.
- Xiang, F., Huang, Y.S., Shi, X.H., and Zhang, Q. (2010). Mitochondrial chaperone tumour necrosis factor receptor-associated protein 1 protects cardiomyocytes from hypoxic injury by regulating mitochondrial permeability transition pore opening. *FEBS J.* **277**, 1929–1938.
- Yoshida, S., Tsutsumi, S., Muhlebach, G., Sourbier, C., Lee, M.J., Lee, S., Vartholomaïou, E., Tatokoro, M., Beebe, K., Miyajima, N., et al. (2013). Molecular chaperone TRAP1 regulates a metabolic switch between mitochondrial respiration and aerobic glycolysis. *Proc. Natl. Acad. Sci. USA* **110**, E1604–E1612.
- Zhang, L., Karsten, P., Hamm, S., Pogson, J.H., Müller-Rischart, A.K., Exner, N., Haass, C., Whitworth, A.J., Winklhofer, K.F., Schulz, J.B., and Voigt, A. (2013). TRAP1 rescues PINK1 loss-of-function phenotypes. *Hum. Mol. Genet.* **22**, 2829–2841.
- Zhao, H., Donnelly, A.C., Kusuma, B.R., Brandt, G.E.L., Brown, D., Rajewski, R.A., Vielhauer, G., Holzbeierlein, J., Cohen, M.S., and Blagg, B.S.J. (2011). Engineering an antibiotic to fight cancer: optimization of the novobiocin scaffold to produce anti-proliferative agents. *J. Med. Chem.* **54**, 3839–3853.
- Zhao, H., Garg, G., Zhao, J., Moroni, E., Girgis, A., Franco, L.S., Singh, S., Colombo, G., and Blagg, B.S.J. (2015). Design, synthesis and biological evaluation of biphenylamide derivatives as Hsp90 C-terminal inhibitors. *Eur. J. Med. Chem.* **89**, 442–466.
- Zhou, C., Zhang, C., Zhu, H., Liu, Z., Su, H., Zhang, X., Chen, T., Zhong, Y., Hu, H., Xiong, M., et al. (2020). Allosteric regulation of Hsp90 α 's activity by small molecules targeting the middle domain of the chaperone. *iScience* **23**, 100857.

STAR★METHODS

KEY RESOURCES TABLE

REAGENT or RESOURCE	SOURCE	IDENTIFIER
Antibodies		
Anti-Myc tag (clone 4A6)	Merck	Cat#05-724; RRID: AB_309938
Mouse monoclonal anti-human TRAP1 (clone TR-1A)	Santa Cruz	Cat#sc-73604; RRID: AB_1130629
Mouse monoclonal anti-rodent TRAP1 (clone 42)	Becton Dickinson	Cat#612344; RRID: AB_399710
Mouse monoclonal anti-SDHA (clone D-4)	Santa Cruz	Cat#sc-166947; RRID: AB_10610526
Mouse monoclonal anti- β actin (clone C4)	Santa Cruz	Cat#sc-47778; RRID: AB_2714189
Rabbit polyclonal anti-TOM20 (clone FL-145)	Santa Cruz	Cat#sc-11415; RRID: AB_2207533
Rabbit polyclonal anti-citrate synthetase	Abcam	Cat#ab96600; RRID: AB_10678258
IRDye® 680LT goat (polyclonal) anti-mouse	LI-COR	Cat#926-68020; RRID: AB_10706161
IRDye® 800CW goat (polyclonal) anti-rabbit	LI-COR	Cat#926-68021; RRID: AB_10706309
Bacterial and Virus Strains		
<i>Escherichia coli</i> ; strain: BL21-AI	Thermo Fisher	C607003
pMDLg/pRRE	Masgras et al., 2017a	Addgene plasmid #12251; RRID: Addgene_12251
pRSV-Rev	Masgras et al., 2017a	Addgene plasmid #12253; RRID: Addgene_12253
pMD2.G	Masgras et al., 2017a	Addgene plasmid #12259; RRID: Addgene_12259
Biological Samples		
Chemicals, Peptides, and Recombinant Proteins		
Human TRAP1	Leskovar et al., 2008	N/A
Human Myc-tagged TRAP1	This paper	N/A
Human Hsp90 α	Enzo Life Sciences	Cat#ADI-SPP-776-D
17AAG	Sigma-Aldrich	Cat#A8476; CAS: 75747-14-7
Radicicol	Santa Cruz	Cat#sc-200620; CAS: 12772-57-5
Compound 1	Vitas-M	Cat#STK031415
Compound 2	Enamine	Cat#Z1128779798
Compound 3	National Cancer Institute (NCI)	Cat#NSC338501; CAS: 26988-58-9
Compound 4	National Cancer Institute (NCI)	Cat#NSC668594
Compound 5	Ambinter	Cat#AMB9798487
Compound 6	Enamine	Cat#Z363507628
Compound 7	National Cancer Institute (NCI)	Cat#NSC56914; CAS: 6947-27-9
Compound 8	Ambinter	Cat#AMB3429185
Compound 9	Vitas-M	Cat#STL380969
Compound 10	National Cancer Institute (NCI)	Cat#NSC1032; CAS: 5336-09-4
Compound 11	National Cancer Institute (NCI)	Cat#NSC151831
Critical Commercial Assays		
Cell Titer 96® Aqueous One Solution	Promega	Cat#G3580
Experimental Models: Cell Lines		
Human: HEK293T	ATCC	CRL-11268
Mouse: sMPNST cells (Nf1 ^{-/-} ; P53 ^{-/-})	Mo et al., 2013	Laboratory of Dr. Lu Q. Le
Mouse: cisMPNST cells (Nf1 ^{-/-} ; P53 ^{-/-})	Vogel et al., 1999	Laboratory of Dr. Lu Q. Le
Human: S462 cells (Nf1 ^{-/-})	Spyra et al., 2011	Laboratory of Dr. Lan Kluwe
Experimental Models: Organisms/Strains		
Zebrafish (<i>Danio rerio</i>); strain: AB (wild-type line)	European Zebrafish Resource Center	ZFIN: ZDB-GENO-960809-7

(Continued on next page)

Continued		
REAGENT or RESOURCE	SOURCE	IDENTIFIER
Oligonucleotides		
Morpholino: MO-TRAP1: GATCGGATCATTCTGCTGTAG	This paper	N/A
Single guide RNA sequence: mouse TRAP1 #1: CACCGCGCCGAAGTCCAGCCAGCGC	Masgras et al., 2017b	N/A
Single guide RNA sequence: mouse TRAP1 #2: CACCGTTTGTGTGGGGCCCTAAC	Masgras et al., 2017b	N/A
Single guide RNA sequence: human TRAP1 #1: CACCGAAAGCTTCTTTGTCTCGGCC	Masgras et al., 2017b	N/A
Single guide RNA sequence: human TRAP1 #2: CACCGCAGTTTTTCCAAGGCATCGC	Masgras et al., 2017b	N/A
Recombinant DNA		
Plasmid: pET151/D-TOPO/TRAP1	Lavery et al., 2014	Laboratory of Dr. David Agard
Plasmid: lentiCRISPRv2	Sanjana et al., 2014	Addgene plasmid #52961; RRID: Addgene_52961
Plasmid: pcDNA3 mito-GFP1-9	Genscript	N/A
Plasmid: pcDNA3-TRAP1-GFP10 modified with the tenth β -strand of sfGFP at the C terminus: EFGGSLEGGGTTMDLPDDHYLSTQTILSK DLNGTDVG	Genscript	N/A
Plasmid: pcDNA3-SDHA-GFP11 modified with the eleventh β -strand of sfGFP at the C terminus: EFSGSGGGSGGGSTSEKRDHMLVLETV TAAGGITDAS	Genscript	N/A
Plasmid: pcDNA3-ATP50-GFP10 modified with the tenth β -strand of sfGFP at the C terminus: EFGGSLEGGGTTMDLPDDHYLSTQT ILSKDLNGTDVG	Genscript	N/A
Software and Algorithms		
MAESTRO	Schrodinger inc.	https://www.schrodinger.com
AMBER16	Amber suite	http://www.ambermd.org/
Discovery Studio	Biovia	https://www.3dsbiovia.com/
ProteOn Manager Software	Bio-Rad	https://www.bio-rad.com/en-it/product/proteon-manager-software
CRISPR design tool	Laboratory of Dr. Feng Zhang	https://zlab.bio/guide-design-resources
Leica LAS AF	Leica Microsystems	https://www.leica-microsystems.com/products/microscope-software/details/product/leica-las-x-ls
ImageJ	National Institutes of Health (NIH)	https://imagej.nih.gov/ij/download.html
FACSDiva software	Becton Dickinson	https://www.bdbiosciences.com/en-us/instruments/research-instruments/research-software/flow-cytometry-acquisition/facsdiva-software
Origin® 8	Origin Lab	https://www.originlab.com/

LEAD CONTACTS AND MATERIAL AVAILABILITY

Further information and requests for resources and reagents should be directed to and will be fulfilled by the Lead Contact, Giorgio Colombo (g.colombo@unipv.it). All unique/stable reagents generated in this study are available from the Lead Contact without restriction.

EXPERIMENTAL MODEL AND SUBJECT DETAILS

Mouse and Human MPNST cell lines

Mouse malignant peripheral nerve sheath tumor (MPNST) sMPNST cells were established from neurofibromin 1 (Nf1)-deficient skin precursors (SKP) (Mo et al., 2013); cisMPNST cells were derived from spontaneous MPNSTs arising in *cis* Nf1^{+/-};P53^{+/-} mice (Vogel et al., 1999); both mouse MPNST cells lines were kindly provided by Dr. Lu Q. Le, University of Texas Southwestern Medical Center, Dallas, TX. Human S462 MPNST cells (Spyra et al., 2011) were generated by Lan Kluwe, University Medical Center, Hamburg, Germany and kindly provided by Conxi Lazaro, Institut Català d'Oncologia, Barcelona, Spain; all cells were grown in Dulbecco's modified Eagle's medium (DMEM) supplemented with 10% fetal bovine serum, 1% glutamine, 1% sodium pyruvate and 1% penicillin and streptomycin at 37°C in a humidified atmosphere containing 5% CO₂.

Animals

Wild-type zebrafish (*Danio rerio*) were maintained in a temperature-controlled room (28.5°C) and fed as described (Kimmel et al., 1995). Fish were kept under a 14 h light – 10 h dark cycle. For mating, males and females were separated in the late afternoon and the next morning were freed to start courtship, which ended with eggs deposition and fecundation. Eggs were collected, washed with fish water (0.5 mM NaH₂PO₄, 0.5 mM NaHPO₄, 0.2 mg/l methylene blue, 3 mg/l instant ocean) and maintained at 28.5°C in fish water supplemented with an antibiotic-antimycotic cocktail (50 µg/ml ampicillin, 100 units/ml penicillin, 0.1 mg/ml streptomycin and 3.3 µg/ml amphotericin B). All experiments with zebrafish larvae were performed in accordance with the European and Italian Legislations.

METHOD DETAILS

Initial Molecular Dynamics Simulations of ATP-bound TRAP1

Initial all-atom MD simulations in explicit water of the mature form of TRAP1 used for the definition of the allosteric site and for the design of the pharmacophore have already been described (Moroni et al., 2018). Briefly, the starting conformation was the high-quality diffracting crystal of the full length dimer of TRAP1 crystallized by Lavery et al., PDB entry 4IPE.pdb (Lavery et al., 2014), in complex with the non-hydrolyzable substrate analog, AMP-PNP. The dimer was solvated in a tetrahedral box and a 1 nm layer of solvent molecules surrounding the protein has been added. The simulated systems eventually contained more than 220000 particles. Such system was simulated in 3 independent replicas of 200 ns each. The three replicas were then combined and analyses were carried out on the combined ensemble of sampled conformations.

Computational identification of allosteric pockets

The hypothesis underlying the identification of potential allosteric pocket implies that these protein regions can be dynamically connected to the catalytic site in the N-terminal domain so that a perturbation at one site reverberates to the other one.

In order to identify distal protein regions that are dynamically connected to the catalytic site we used the previously introduced distance fluctuation analysis. For the MD meta-trajectory, we computed the matrix of distance fluctuations, using the equilibrated part of each trajectories (time interval 25–200 ns), in which each element of the matrix corresponds to the CP parameter (Moroni et al., 2018; Morra et al., 2012):

$$CP_{ij} = \langle (d_{ij} - \langle d_{ij} \rangle)^2 \rangle \quad (1)$$

where d_{ij} is the (time-dependent) distance of the C α atoms of amino acids i and j , and the brackets indicate the time-average over the trajectory. This parameter is invariant under translations and rotations of the molecules and, unlike the covariance matrix, does not depend on the choice of a particular protein reference structure.

The CP matrix can be used to assess the intrinsic flexibility of proteins and how it changes upon ligand binding. CP was calculated for any pair of residues during the trajectory. This parameter is able to identify residues that move in a highly coordinated fashion, and it reflects the presence of specific coordination patterns and quasi-rigid domains motion in the protein of interest. In particular, pairs of amino acids belonging to the same quasi-rigid domain are associated with small distance fluctuations and vice versa.

In order to identify residues distant from the nucleotides binding site which display high coordination with it despite their physical separation, we set as threshold for the distance fluctuation the value obtained calculating the average local fluctuation d_{ij} between every C α atom of residue i and the C α atoms of neighboring residues j having an average distance from residue i lower than 7 Å. This is a parameter that describes the local dynamics. Residues that are apart and move with a CP_{ij} that characterizes the local motion can be considered to move in a coordinated way.

Next, the program SiteMap (Schrödinger Release 2015-4: SiteMap, Schrödinger, LLC, New York, NY, 2015) was used to verify if the identified residues have the properties that characterize drug-binding sites, which can be targeted by small ligands. The program analyzes the entire protein to locate potential binding sites and through the evaluation of their size, functionality and extent of solvent exposure, it assess a site's propensity for ligand binding, and eliminates those not likely to be pharmaceutically relevant. In order to verify whether this potential binding site is present in all the relevant protein conformations, we carried out this analysis on the

representative structures of the most populated clusters obtained from the cluster analysis of the MD meta-trajectory. The cluster analysis was carried out using the method described by Daura and co-workers (Daura et al., 1999) with a cutoff of 0.2 nm on the entire protein. Individual frames were grouped into 19 clusters, with the most populated four accounting for 81% of the structural diversity. The four conformations were analyzed using SiteMap with the default parameters, showing that the selected residues are part of a druggable binding pocket and that this pocket is consistently present in all the protein conformations considered.

Pharmacophore development and virtual screening

The MD meta-trajectory was used to define 3D pharmacophore features of a pharmacophore hypothesis for the putative allosteric pocket. In order to take into account the different location of the chemical groups that characterize the pocket during the MD simulation, the pharmacophore was generated using the protein conformations of the most four populated clusters obtained from the trajectory through cluster analysis.

The pharmacophore model was created using these four protein conformations, in a way that would feature a projection point where a donor group could establish a hydrogen-bond with the side chains of Glu647 and Glu648. Then, an acceptor feature pointing toward the positive charged zone formed by residue Arg341, Lys364 and Arg370 was introduced, together with another donor feature in proximity of the negative protein area formed by Glu457 and Asp458. A hydrophobic feature was placed such that it could complement the large hydrophobic pocket that characterizes the putative binding site. We then introduced an additional acceptor feature that points toward the side chain of Arg644 and Gln640, separating the hydrophobic pocket from the negative zone formed by Glu647 and Glu648. Finally, we added an acceptor feature pointing toward the hydrophobic pocket, in order to engage favorable hydrogen bond interactions with the backbone of the surrounding amino acids.

As mentioned above, in order to take into account protein flexibility, we used fluctuations in the positions and distances of the different functionalities from the MD simulations described (Moroni et al., 2018) in order to determine the upper and lower boundaries in the positioning of the hydrogen-bond donor/acceptor functions of the pharmacophore. We used these values to define the radius tolerances for every feature, ranging from 1.2 to 1.7 Å, i.e., the spherical volume where matching chemical groups could be located. We carried out shape filtering for representing the steric aspect of the protein by manually selecting all residues of the binding site and adding the corresponding excluded volume spheres of radius 1.2 Å.

We utilized the resulting pharmacophore model to perform a screening search of the NCI repository, requiring a minimum of 3 matching features. Using this criterion the pharmacophore returned 12572 molecules. We used the same pharmacophore model for the screening of the ZINC database, which had previously been filtered to consider only drug-like molecules. The actual screening was performed on 2,500,000 compounds, resulting in 55318 molecules matching the pharmacophore query using the same request on the minimum matching features.

We then ranked molecules according to the FitValue of the Pharmacophore Tools module of BIOVIA, a measure of how well the ligand fits the pharmacophore (the higher the fit score, the better the match), selecting only those molecules with FitValue higher than 4. The resulting molecules were next processed using the LigPrep module of the Schrodinger Suite with the default parameters.

The resulting structures were post-processed by using the QikProp (Schrödinger Release 2015-4: QikProp, Schrödinger, LLC, New York, NY, 2015.) program running in normal mode. Qikprop generates physically relevant descriptors, and uses them to calculate a set of ADMET-related properties. The overall drug-likeness parameter (#star) was used to assess the pharmacokinetic profiles of the compounds. This parameter indicates the number of property descriptors computed by QikProp that fall outside the optimum range of values for 95% of known drugs. Molecules having this parameter lower than 3 and fully satisfying the Lipinski Rule of Five were kept for the next step.

These selected molecules were then docked with the GLIDE docking program (Glide, version 6.9, Schrödinger, LLC, New York, NY, 2015) on the putative allosteric site of TRAP1. Rigid receptor and flexible ligand docking calculations were performed in standard precision mode (SP) with the OPLS_2005 force field, nonplanar conformations of amide bonds were penalized, van der Waals radii were scaled by 0.80, and the partial charge cutoff was fixed to 0.15. No further modifications were applied to the default settings. The best docking poses according to the docking score function were superimposed rigidly with the pharmacophore model and visually inspected in order to verify the matching between the docking pose and the chemical features of the pharmacophore. 39 molecules were then selected based on this criterion from the virtual screening hits, 11 of these being available for experimental evaluation.

Molecular Dynamics simulations of the allosteric inhibitor-bound TRAP1 complexes

The best docking poses of the active compounds **5**, **6**, and **7** in the TRAP1 allosteric site were taken as starting structures for All-atom Molecular Dynamics. The initial protein conformation corresponded to the most representative cluster obtained from the first set of simulations on the double-ATP state. Each TRAP1-ligand system was simulated in 3 independent replicates. As a control, 3 additional replicates of the TRAP1 double-ATP state were built and simulated in absence of inhibitors. A total of 12 systems were prepared and solvated using the TIP3P parameterization (Jorgensen et al., 1983) for water molecules using the AMBER 16 suite of programs (Case et al., 2017). Each trajectory was simulated for 300 ns each under periodic boundary conditions using the AMBER ff99SB forcefield (Lindorff-Larsen et al., 2010).

Briefly, the dimer was explicitly solvated in an isometric truncated octahedral box and buffered with 1 nm layer of solvent. The systems were neutralized with ions and contained on average 200000 particles. To relax the structures 2000 steps of steepest descent were followed by another 2000 steps of conjugate gradient energy minimization. The temperature of the systems was gradually

raised to 300 K in the NVT ensemble in 1.2 ns at 1 fs time-step, using the Langevin thermostat. Six runs of 200 ps were performed increasing the temperature of 50 K at each step. At 300 K, the density of the system was adjusted with 1 ns at 2 fs time-step under NPT conditions by weak coupling to a bath of constant pressure ($P_0 = 1$ bar, coupling time $\tau_p = 0.5$ ps). The production runs were thus carried out in the NVT ensemble. The use of the SHAKE algorithm (Miyamoto and Kollman, 1992) on hydrogen atoms allowed a time step of 2 fs. Electrostatic forces were computed using the particle mesh Ewald algorithm with a truncation cutoff of 8 Å (Darden et al., 1993). The initial velocity of all atoms were obtained from a Maxwellian distribution at the initial temperature of 300 K. To avoid memories of the initial structure and allow for system equilibration, we discarded the first 100 ns for each replicate. A total of 600 ns of productive statistics was accumulated for each ligand-bound and ligand-free TRAP1 system.

Long- and short-range communication analysis of the allosteric inhibitor-bound TRAP1 complexes

The Communication Propensity (CP) analysis was separately performed on each of the 12 systems via the calculation of the CP matrix (Moroni et al., 2018; Morra et al., 2012). To identify TRAP1 residues involved in long-range communication with the ATP binding pocket, we extracted from the CP matrixes those residues which, despite being more than 40 Å apart, displayed CP values below their specific threshold associated to local fluctuation (LF). To get more robust results and unify the information collected over individual replicates, we filtered out from the total set of connected residues only those pairs which consistently show long-range coupling in at least 2 out of 3 replicates for each simulated TRAP1 state.

The extent of mechanical coordination between the 2 N-terminal strap elements (the segment 85-101) with other protein residues was also assessed at shorter distances for each individual system setting the cutoff to 7 Å. This strategy allowed to identify the whole set of residues connected to the N-terminal straps just above the distance that defines their local environment. The information obtained on each replicate of a generated TRAP1 state was then merged in a single set of strap-connected residues. Similarly, we took as informative only the residue pairs that were consistently connected in at least 2 out of 3 replicates for each system. The degree of coupling was specifically assessed between the 2 straps and the NTDs in each simulated TRAP1 state and it is presented as a percentage over the total number of consistently connected residues.

Cluster analysis of ligand conformations

The cluster analysis was performed through the “nearest neighbor” algorithm implemented in an in-house script. Only the last 200 ns of production run was used to identify the main binding modes in the 3 replicates of compounds **5**, **6** and **7**. Each meta-trajectory of 600 ns was fitted on the backbone atoms of residues displaying a maximum occupancy time greater than 120 ns (> 20% of the total production time) (Table S1). A matrix of RMSD between each pair of ligand structures was generated and used to find the best partitioning. The optimal cutoff for the cluster analysis was chosen by calculating the Davies-Bouldin validity index (DBI) every 0.15 Å between the first peak and the first minimum of the RMSD distribution. The DBI index is defined as an internal evaluation metric for clustering. It is an average over the number of clusters of the ratio between the maximum scatter within a cluster and the minimum distance between two representative cluster centers (medoid). Table S2 provides information on the cluster analysis performed for compounds **5**, **6** and **7**.

Production and purification of recombinant human TRAP1

The expression and purification of human TRAP1 were carried out as described previously (Lavery et al., 2014). The mature sequence of TRAP1 (residues 60-704), without the mitochondrial targeting sequence, was cloned into the pET151/D-TOPO plasmid (Invitrogen, Grand Island, NY), resulting in a N-terminally His-tagged TRAP1 fusion protein expressed into *E. coli* BL21-AI. Protein synthesis was induced with 1 mM isopropyl- β -D-thiogalactopyranoside and 0.2% arabinose when bacteria grown at 30°C in Luria-Bertani broth supplemented with 0.4% glucose reached an OD600 of 0.7-0.8. After induction, cells were grown at 16°C for 20 h and harvested by centrifugation. The bacterial pellet was resuspended in binding buffer (50 mM potassium phosphate, pH 8.0, 500 mM sodium chloride, 20 mM imidazole, 3 mM β -mercaptoethanol), sonicated on ice after addition of 0.2 mM phenylmethylsulfonyl fluoride and centrifuged at 20000 *g*. The soluble fraction was filtered and incubated with Ni-NTA (GE Healthcare Biosciences, Pittsburgh, MA) under rotation for 1 hour at 4°C. Lysate was then loaded onto a gravity column and the His-tagged protein was eluted in a buffer composed by 50 mM potassium phosphate, pH 8.0, 300 mM sodium chloride, 500 mM imidazole, 3 mM β -mercaptoethanol. The eluted protein was dialyzed overnight (dialysis buffer: 10 mM Tris-HCl pH 8.0, 200 mM sodium chloride, 1 mM DTT) and the 6x-His-tag was cleaved using TEV protease (Sigma-Aldrich, St. Louis, MO). The fractions containing human TRAP1 were pooled and stored at -80°C at a concentration of 1 mg/ml.

Measurement of TRAP1 and Hsp90 ATPase activities

TRAP1 and Hsp90 ATPase activities were measured using the previously described ATP-regenerating assay (Leskovar et al., 2008) on a microplate spectrophotometer (Infinite® 200 PRO, Tecan, Switzerland) at 340 nm. Both activities were determined in an assay buffer (50 mM Tris-HCl pH 7.4, 50 mM Sucrose, 50 mM potassium chloride, 4 mM magnesium chloride, 2 mM EGTA) supplemented with 1.5 mU/mL L-lactate dehydrogenase, 0.8 mU/mL pyruvate kinase, 300 μ M NADH and 2 mM phosphoenolpyruvate using 450 ng human recombinant Hsp90 α (Enzo Life Sciences, Farmingdale, NY) or TRAP1. The reaction was initiated after the addition of ATP (200 μ M for TRAP1 and 1 mM for Hsp90 α) and the protein activity was measured following NADH oxidation for 1 h at 37°C. Both Hsp90 and TRAP1 inhibitors were added immediately before starting measurements.

Measurement of kinetic constants with surface plasmon resonance (SPR)

SPR measurements were performed with Biacore T100 biosensor system (GE Healthcare Biosciences) using a CM5 sensor chip. Prior to each run, anti-Myc tag antibody (Merck KGaA) diluted into a buffer containing 10 mM HEPES, pH 7.4, and 150 mM NaCl to a final concentration between 10 and 50 $\mu\text{g/ml}$ was immobilized on a CM5 sensor chip after activation with N-ethyl-N'-[[dimethylamino]propyl]carbodiimide (EDC) in the presence of N-hydroxysuccinimide (NHS). After antibody immobilization, a 10-min injection of 1M ethanolamine, pH 8.5, at 5 $\mu\text{l/min}$ was performed in order to quench excessive activated succinimide ester groups. Using HBS (10 mM HEPES pH 7.4, 150 mM NaCl and 3 mM EDTA) as running buffer, equimolar amounts of human recombinant TRAP1, previously modified with a Myc tag at the level of the CTD, were captured by the anti-Myc antibody attached to the surface of the sensor chip. Compound 5 was then injected at increasing concentrations (39, 78, 156, 313, 625 and 1250 μM). Unspecific binding and buffer interactions were subtracted from each sensorgram and the resulting curves were fitted using a Langmuir interaction model (ProteOn Manager Software, Bio-Rad Laboratories, Hercules, CA) to obtain binding constants.

Generation of TRAP1 knock-out MPNST cell lines

TRAP1 knock-out cells were generated by using the clustered regulatory interspaced short palindromic repeat (CRISPR)-Cas9 gene system (Sanjana et al., 2014). Sequences for the single guides (for mouse TRAP1: 5'-CACCGCGCCGAAGTCCAGCCAGCGC-3' and 5'-CACCGTTTGTGTGGGGCCCCTAAC-3'; for human TRAP1: 5'-CACCGAAAGCTTCTTGTCTCGGCC-3' and 5'-CACCGCAGTTTTCCAAGGCATCGC-3') were obtained by using the CRISPR design tool (<http://www.crispr.mit.edu>). Scrambled single guides were used as negative controls. Oligonucleotide pairs were annealed and cloned into the transfer plasmid lentiCRISPRv2 (Addgene, #52961) and co-transfected with the packaging plasmids pMDLg/pRRE (Addgene, #12251), pRSV-Rev (Addgene, #12253) and pMD2.G (Addgene, #12259) into human embryonic kidney (HEK) 293T cells for viral production. Recombinant virus was collected and used to infect cells by standard methods. Infected cells were then selected with 1 $\mu\text{g/ml}$ puromycin.

Knockdown of TRAP1 in wild-type zebrafish embryos

TRAP1 knockdown zebrafish embryos were obtained by injecting the 5'-GATCGGATCATTCTGCTGCTGTAG-3' TRAP1 morpholino (1.0 $\mu\text{g}/\mu\text{l}$) in wild-type embryos at 1-4 cell stage using a WPI pneumatic PicoPump PV820 injector. At 96 hours post-fertilization, wild-type and TRAP1 knockdown zebrafish larvae were treated with either DMSO or compound 5 (100 μM , 4 hours) before measuring the SQR activity of SDH as described below. Both DMSO and TRAP1 inhibitor were added directly to fish water.

TRAP1-SDHA interaction assays

sgTRAP1 sMPNST cells were grown on microscope slides and co-transfected with plasmids pcDNA3GFP1-9, pcDNA3-TRAP1-GFP10 and pcDNA3-SDHA-GFP11. The pcDNA3 mito-GFP1-9 plasmid was synthesized by Genscript (Piscataway, NJ) with optimized mammalian codons based on the amino acid sequence of sfGFP1-9 (Cabantous et al., 2013; Koraiichi et al., 2018) and fused to N terminus with a mitochondrial targeting sequence derived from the subunit VIII of human cytochrome c oxidase.

The plasmid pcDNA3-TRAP1-GFP10 encoding for TRAP1 was modified with the tenth β strand of sfGFP at the C terminus (EFGGSLEGGGTTMDLPDDHYLSTQTILSKDLNGTDVG) and plasmid pcDNA3-SDHA-GFP11 encoding for SDHA was modified with the eleventh β strand of sfGFP at the C terminus (EFGSGGGSGGGSTSEKRDMVLETVTAAGGITDAS). In selected experiments, the plasmid pcDNA3-ATP50-GFP10 encoding for OSCP protein modified with the tenth β strand of sfGFP at the C terminus (EFGGSLEGGGTTMDLPDDHYLSTQTILSKDLNGTDVG) and plasmid pcDNA3-SDHA-GFP11 were used as negative control, showing no interaction (data not shown). When indicated, compound 5 (100 μM) was added 5 hours after transfection. Cells were stained with Mitotracker red (50 nM, 30 min) 48 hours after transfection to detect the mitochondrial network, fixed with 4% PFA, visualized with a fluorescence Leica DMI600B microscope (20x objective) and analyzed using LAS AF (Leica Microsystems, Wetzlar, Germany) and ImageJ® software (National Institutes of Health, University of Wisconsin, WI). Images from individual GFP⁺-sMPNST cells were acquired with a LSM 700 (Zeiss, Oberkochen, Germany) confocal microscope. Percentage of cells showing interaction between TRAP1 and SDHA was calculated as the ratio between green (GFP⁺) and red (total) cells; at least 2,000 cells were analyzed for each condition.

Cell fractionation and immunoblotting

Cells and zebrafish larvae were lysed at 4°C in EB buffer (150 mM sodium chloride, 20 mM Tris-HCl pH 7.4, 5 mM EDTA, 10% glycerol, 1% Triton X-100) supplemented with protease and phosphatase inhibitors (Sigma-Aldrich). Crude lysates were cleared by centrifuging for 25 min at 20000 g and proteins were quantified using a BCA Protein Assay Kit (Thermo Fisher Scientific, Waltham, MA). Protein lysates were boiled in Laemmli sample buffer, separated in reducing conditions on 4%–12% Bis-Tris NuPage gels (Life Technologies, Carlsbad, CA), transferred onto Amersham Protran 0.2 NC nitrocellulose membranes (GE Healthcare Biosciences) following standard methods. Primary antibodies were incubated for 16 h at 4°C and IRDye® 680LT goat (polyclonal) anti-mouse and IRDye® 800CW goat (polyclonal) anti-rabbit secondary antibodies were added for 2 h at room temperature. Proteins were visualized with an Odyssey CLx Imaging System (LI-COR Biosciences, Lincoln, NE). Anti human TRAP1, anti SDHA and anti β -actin mouse monoclonal antibodies and anti TOM20 rabbit polyclonal antibody were all from Santa Cruz; anti rodent TRAP1 mouse monoclonal antibodies was from Becton Dickinson; anti citrate synthase rabbit polyclonal antibody was from Abcam.

Measurement of succinate:coenzyme Q reductase (SQR) activity of succinate dehydrogenase (SDH)

The SQR enzymatic activity of SDH was measured either in neoplastic cells or in zebrafish embryos. Samples were collected and lysed at 4°C in a buffer composed by 25 mM potassium phosphate, pH 7.2, and 5 mM magnesium chloride containing protease and phosphatase inhibitors. Cell (40 µg protein per trace) and zebrafish homogenates (60 µg per trace) were then pre-incubated for 10 minutes at 30°C in the presence of 20 mM sodium succinate and 10 µM alamethicin. Reaction was started by the addition of 5 mM sodium azide, 5 µM antimycin A, 2 µM rotenone, 100 µM 2,6-dichlorophenolindophenol (DCPIP) and 65 µM coenzyme Q1. SQR enzymatic activity was measured following the reduction of DCPIP at 600 nM ($\epsilon = 19.1 \text{ mM}^{-1} \text{ cm}^{-1}$); each measurement was normalized for protein amount.

Cell viability assays

Cell viability was assessed either by a colorimetric MTS assay (Cell Titer 96® Aqueous One Solution; Promega, Madison, WI) or by flow cytometry analysis. For MTS measurements, plates were incubated at 37°C overnight and read in a microplate spectrophotometer (Infinite® 200 PRO). Flow cytometry recordings were performed as described previously (Ciscato et al., 2014; Guzzo et al., 2014). Briefly, cells were stained with FITC-conjugated Annexin-V and 7-Aminoactinomycin D (7-AAD) to determine phosphatidylserine exposure on the cell surface (increased FITC-conjugated Annexin-V staining) and loss of plasma membrane integrity (7-AAD permeability and staining). Cells were incubated at 37°C in an assay buffer containing 135 mM sodium chloride, 10 mM HEPES, 5 mM calcium chloride and then samples were analyzed on a FACS Canto II flow cytometer (Becton Dickinson, Franklin Lakes, New Jersey). Data acquisition and analysis were performed using FACSDiva software.

Cell proliferation assays

Proliferation was assessed by plating cells in 12-well dishes with an initial seeding density of 1×10^4 cells per well. Cells were allowed to settle overnight and one dish was counted to determine the starting cell number. Cells in the remaining dishes were incubated with either DMSO or the TRAP1 inhibitors at the indicated concentration. Cell counts were performed in the four subsequent days using a Fuchs-Rosenthal chamber.

In vitro tumorigenesis assays

Focus forming assays were performed on cells grown in 12-well culture plates in DMEM medium supplemented with 10% fetal bovine serum. When cells reached sub-confluence, serum concentration was decreased to 1% and TRAP1 inhibitors were added at the indicated concentrations. At the 10th day after serum decrease, plates were washed in PBS, fixed in methanol for 30 min, stained with GIEMSA solution for 1h and analyzed with ImageJ software.

QUANTIFICATION AND STATISTICAL ANALYSIS

Data were analyzed and presented as mean \pm standard error of the mean (SEM) in all figures. Pairs of data groups were analyzed using paired and unpaired two-tailed Student's t tests. In the case of more than two groups, one-way analysis of variance (ANOVA) followed by Bonferroni post hoc test was applied. Statistical significance was determined using Origin® 8 (OriginLab, Northampton, MA). Results with a p value lower than 0.05 were considered significant; ***p < 0.001, **p < 0.01, *p < 0.05 compared to controls. Each experiment was repeated at least three times.

DATA AND CODE AVAILABILITY

Data, C-programs and Python scripts for analysis of coordination in molecular dynamics simulations are available upon request.